

This work was written as part of one of the author's official duties as an Employee of the United States Government and is therefore a work of the United States Government. In accordance with 17 U.S.C. 105, no copyright protection is available for such works under U.S. Law.

Public Domain Mark 1.0

<https://creativecommons.org/publicdomain/mark/1.0/>

Access to this work was provided by the University of Maryland, Baltimore County (UMBC) ScholarWorks@UMBC digital repository on the Maryland Shared Open Access (MD-SOAR) platform.

**Please provide feedback**

Please support the ScholarWorks@UMBC repository by emailing [scholarworks-group@umbc.edu](mailto:scholarworks-group@umbc.edu) and telling us what having access to this work means to you and why it's important to you. Thank you.

# A global MHD solar wind model with WKB Alfvén waves: Comparison with Ulysses data

Arcadi V. Usmanov

Institute of Physics, University of St. Petersburg, St. Petersburg, Russia

Melvyn L. Goldstein

NASA Goddard Space Flight Center, Greenbelt, Maryland

Bruno P. Besser and Johannes M. Fritzer

Space Research Institute, Austrian Academy of Sciences, Graz, Austria

**Abstract.** We use a steady state global axisymmetric MHD model to reproduce quantitatively the Ulysses observations during its first fast latitude traversal in 1994–1995. In particular, we are able to account for the transformation of a surface dipole magnetic field near the Sun into the configuration observed at large heliocentric distances. The MHD equations are solved by combining a time relaxation numerical technique with a marching-along-radius method. We assume that Alfvén waves, propagating outward from the Sun, provide additional heating and acceleration to the flow. Only solutions with waves reproduce the plasma parameters observed in the high-latitude fast solar wind. We show that the meridional distribution of solar wind plasma and magnetic field parameters is dominated by two processes. First, inside  $\sim 24 R_{\odot}$  both the plasma velocity and magnetic field relax toward a latitude-independent profile outside the equatorial current sheet (where magnetic forces dominate over thermal and wave gradient forces). Second, outside  $\sim 24 R_{\odot}$  there is another meridional redistribution due to a poleward thermal pressure gradient that produces a slight poleward gradient in the radial velocity and an equatorward gradient in the radial component of the magnetic field. We reproduce the observed bimodal structure and morphology of both fast and slow wind and show that computed parameters are generally in agreement with both in situ data and conditions inferred to be characteristic of the solar corona.

## 1. Introduction

The structure of the solar corona and solar wind results from the interaction between outward streaming coronal plasma and magnetic fields. In the inner corona the bulk speed of the plasma is both subsonic and sub-Alfvénic. Consequently, at the photosphere, magnetic forces dominate pressure gradients and gravitation and determine the large-scale structure of the expanding and accelerating solar corona as the flow becomes supersonic and super-Alfvénic. Fast wind is associated with coronal holes within which the magnetic field is unipolar and open, while low-speed wind appears to originate above and at the boundaries of the coronal streamers where the magnetic fields are bipolar, which forces the plasma to flow around regions where the field strength is sufficient to stagnate the flow.

In this paper we incorporate self-consistently Alfvén waves into a two-dimensional simulation of the solar corona and solar wind in the region from  $1 R_{\odot}$  (solar radius) to 5 AU. We solve numerically the governing MHD equations in spherical coordinates for a surface dipole magnetic field. Alfvén waves of solar origin are invoked explicitly to heat and accelerate the solar wind. Because we are interested mainly in computing the global coronal structure rather than in modeling details of the transformation of momentum and energy from the waves to the flow [cf. *Ofman and Davila*, 1995, 1997, 1998; *Ruderman et al.*, 1999], we use the short-wavelength Wentzel-Kramers-Brillouin (WKB) approximation. We find that the model reproduces many aspects of the Ulysses observations of fast and slow solar wind during the fast latitude traversal in 1994–1995.

The problem of self-consistent modeling of the plasma-magnetic field interaction in the solar corona was studied first by *Pneuman and Kopp* [1971], who used an iterative technique to solve the steady state MHD equations for a surface dipole magnetic field. *Endler* [1971],

Copyright 2000 by the American Geophysical Union.

Paper number 1999JA000233.  
0148-0227/00/1999JA000233\$09.00

using a time relaxation method, extended the results of *Pneuman and Kopp* to include Ohmic dissipation. The problem has been studied in two dimensions [*Steinolfson et al.*, 1982; *Robertson*, 1983; *Washimi et al.*, 1987; *Cuperman et al.*, 1990; *Wang et al.*, 1993; *Usmanov*, 1993a; *Stewart and Bravo*, 1996, 1997; *Wang et al.*, 1998; *Suess et al.*, 1999] and in three dimensions [*Linker et al.*, 1990; *Usmanov*, 1993b, c; *Linker and Mikić*, 1995; *Mikić and Linker*, 1996; *Linker et al.*, 1999]. (Also see, T. I. Gombosi et al., Multiscale simulation of the solar wind, the magnetosphere, and their disturbance by a coronal mass ejection, submitted to *Journal of Atmospheric and Solar-terrestrial Physics*, 2000.) A surface dipole magnetic field at  $1 R_{\odot}$ , as used in the majority of these studies, is the simplest configuration that has both open (near the pole of the dipole) and closed (near its equator) magnetic field geometry. This choice allows simulation of both coronal-hole-like and streamer-like flows.

The studies referenced above have successfully revealed many features of the magnetic field and plasma distribution in the inner solar corona. Although the main patterns of the solutions based on the MHD equations correspond reasonably well to the magnetic field and plasma observations in the solar wind [e.g., *Usmanov*, 1993a, b, c], MHD models have been unable to account for fast solar wind without incorporating additional extended sources of momentum and energy [*Munro and Jackson*, 1977; *Barnes et al.*, 1995]. One candidate for this source of additional acceleration is a flux of Alfvén waves propagating outward from the Sun. In this paper we explore the consequences of such a flux of waves and do not consider alternative possibilities (such as, for example, those discussed by *Parker* [1990, 1991]).

The importance to the energetics of the corona and solar wind of Alfvén waves has been recognized since their discovery [*Coleman*, 1968; *Unti and Neugebauer*, 1968; *Belcher et al.*, 1969]. *Belcher* [1971] and *Alazraki and Couturier* [1971] pointed out that Alfvén waves should create an additional pressure that would contribute to accelerating the solar wind. Evidence that Alfvén waves are the primary cause of heating and accelerating the solar wind is, however, far from definitive. As pointed out by *Roberts* [1989] and *Smith et al.* [1995b], there appears to be insufficient energy in the observed waves to have both accelerated and heated the wind to the values observed at 0.3 AU by *Helios* and throughout the polar heliosphere by *Ulysses*. One possibility for hiding additional wave energy is a population of high-frequency waves in the corona that would be damped by ion cyclotron absorption as the magnetic field magnitude decreases with radius [*Axford and McKenzie*, 1992; *Tu and Marsch*, 1997]. Evidence that additional wave energy exists in the corona comes from several observations [see, e.g., *Hassler et al.*, 1990; *Ofman et al.*, 1999]. Observations of large velocity fluctuations may indicate the presence of a larger energy flux

of Alfvén waves than would be expected from the WKB extrapolation.

There exist a number of solar wind models that incorporate Alfvén waves in the solar wind momentum and energy balance [e.g., *Hollweg*, 1973, 1978; *Jacques*, 1978; *Heinemann and Olbert*, 1980; *Holzer et al.*, 1983; *Essex et al.*, 1986; *Withbroe*, 1988; *Wang*, 1993a; *Lau and Siregar*, 1996; *McKenzie et al.*, 1995, 1997; *Ong et al.*, 1997]; however, these models are one-dimensional (except for that of *Ong et al.* [1997], who solved a two-dimensional MHD problem for a single magnetic flux tube) and therefore cannot account consistently for nonradial variations in the magnetic field and flow parameters. This paper explores, in a two-dimensional calculation, the effect of an Alfvén wave flux on the flow properties of the solar wind.

The plan of the paper is as follows: Section 2 summarizes some of the observations most relevant to this study and compares them with some previous modeling efforts. In section 3 we describe the governing equations, and in section 4 we discuss in detail the initial and boundary conditions used. The results of simulation are discussed in section 5, and a detailed comparison of the model calculations with *Ulysses* observations is given in section 6. A summary in section 7 concludes the paper.

## 2. Ulysses Observations and Comparison With Previous Models

The magnetic field and plasma observations from *Ulysses* during its fast latitude transit from south pole to north pole during September 1994 to July 1995 showed that the entire heliosphere at solar latitudes  $\gtrsim 20^\circ$  was occupied by two fast unipolar flows separated by a band of slower wind centered near the solar equator [*Phillips et al.*, 1995; *Forsyth et al.*, 1996]. These observations were made at heliocentric distances of 1.3–2.3 AU and at a time just prior to solar activity minimum when large coronal holes covered the polar regions of the Sun. During this period the heliospheric current sheet (HCS) was approximately aligned with the solar equatorial plane and the heliosphere was nearly azimuthally and north-south symmetric [*Phillips et al.*, 1995; *Forsyth et al.*, 1996]. The *Ulysses* observations revealed a sharp boundary between fast and slow wind and no pronounced dependence of plasma and magnetic field parameters on latitude in the fast solar wind. In the fast flows the velocity was  $\sim 700$ – $800 \text{ km s}^{-1}$  (on average,  $773 \text{ km s}^{-1}$  [*Feldman et al.*, 1996]), with a slight positive poleward gradient, while the density and the radial magnetic field were roughly uniform. The mean values of the number density and radial magnetic field, when scaled to 1 AU assuming an  $r^{-2}$  dependence, were  $2.47 \text{ cm}^{-3}$  (poleward of  $\pm 60^\circ$ ) and  $3.02$  ( $-3.17$ ) nT in the northern (southern) fast wind between  $40^\circ$  and  $80^\circ$ , respectively [*Feldman et al.*, 1996; *Forsyth et al.*, 1996]. The slow wind extended in latitude from  $-22^\circ$  to  $+21^\circ$ .

Near solar minimum the dominant component of the solar source magnetic field is a dipole nearly aligned with the solar rotation axis [Hoeksema and Scherrer, 1985; Hoeksema, 1991; Zhao and Hoeksema, 1996]. Using potential field source surface models to extrapolate a dipole field into the heliosphere [Schatten *et al.*, 1969; Hoeksema and Scherrer, 1985; Hoeksema, 1991] yields a radial magnetic field  $B_r$  that increases from equator to pole. Ulysses, however, found no evidence of a significant latitudinal gradient in  $B_r$ , indicating that the magnetic flux was transported to lower latitudes and that heliospheric currents were confined to a relatively narrow HCS.

Classic potential and force-free models that require a pure radial magnetic field outside the source surface are not in agreement with Ulysses observations unless one adds ad hoc currents to create the HCS [Wolfson, 1985; Wang, 1993b; Zhao and Hoeksema, 1995a]. A current sheet extending to large heliocentric distances, however, is an intrinsic feature of calculations based on self-consistent MHD [e.g., Pneuman and Kopp, 1971; Endler, 1971; Robertson, 1983; Bravo and Stewart, 1996].

Another advantage of two- and three-dimensional MHD modeling is the ability to compute self-consistently the expansion of magnetic flux tubes by taking into account the pressure balance between adjacent flow tubes. Otherwise, the expansion factor  $f_s$  (the ratio of the solid angles subtended by a flux tube at some distance from the Sun and at the coronal base) must be treated as a free parameter (in one-dimensional models) or must be computed assuming a potential or force-free magnetic field [Durney and Pneuman, 1975; Levine *et al.*, 1977; Wang and Sheeley, 1990]. Because the geometry of magnetic flux tubes coincides with that of flow tubes when the flows are steady in the corotating frame of reference,  $f_s$  is a critical parameter in solar wind modeling [Kopp and Holzer, 1976; Whang and Chien, 1978]. Ulysses data indicate that there is a non-radial expansion of the solar corona [Smith and Balogh, 1995; Gosling *et al.*, 1995; Roberts and Goldstein, 1998], which implies that one must include transverse momentum in simulations of the heliosphere [Suess *et al.*, 1977; Withbroe, 1989; Suess and Smith, 1996].

To date, a number of simulation studies based on multidimensional MHD solutions have tried, with varying success, to match Ulysses observations. For example, Pizzo and Gosling [1994] solved the three-dimensional MHD equations outside 0.15 AU to study the formation of corotating interaction regions (CIRs). Sittler and Guhathakurta [1999] developed a two-dimensional MHD model which uses as input electron density profiles derived from white light coronagraph data and Ulysses density measurements. This is a semiempirical model in which the magnetic field is prescribed. Mikić and Linker [1996] and Mikić *et al.* [1999], using three-dimensional simulations, compared the position of the HCS to Ulysses observations but could not pro-

duce truly fast wind. Bravo and Stewart [1996] and Stewart and Bravo [1997] constructed an axisymmetric model with collisional heat conduction (similar to that of Robertson [1983]) and used Ulysses plasma observations to specify the boundary conditions at 1 AU, but the plasma densities at  $r = 1 R_\odot$  that they computed are far too small ( $10^5$ – $10^6 \text{ cm}^{-3}$ ) to match typical values derived from observations ( $10^7$ – $10^8 \text{ cm}^{-3}$  [e.g., Koutchmy, 1977]). Using the two-dimensional MHD model of Wang *et al.* [1993], Suess and Smith [1996] [also see, Suess *et al.*, 1999] showed that the gradient in  $B_r$  weakens considerably from  $1 R_\odot$  to a distance of  $5 R_\odot$ . Their model is confined to the solar corona and does not include Alfvén waves. Bravo and Stewart obtained a similar result for the region  $1$ – $10 R_\odot$ .

### 3. Governing Equations and Description of the Model

We consider a system composed of a background coronal plasma together with Alfvén waves in the short-wavelength WKB approximation, that is, we assume that variations of the background are small over distances comparable with the wavelengths of the Alfvén waves. We assume also that the Alfvén waves are subject to a dissipation characterized by a damping length  $L$ . The resulting time-dependent, single-fluid, polytropic MHD equations are [Jacques, 1977, 1978]

$$\frac{\partial \rho}{\partial t} + \nabla \cdot \rho \mathbf{u} = 0, \quad (1)$$

$$\frac{\partial \mathbf{u}}{\partial t} + (\mathbf{u} \cdot \nabla) \mathbf{u} = -\frac{1}{\rho} \nabla P - \frac{GM_\odot}{r^2} \hat{\mathbf{r}} + \frac{1}{4\pi\rho} (\nabla \times \mathbf{B}) \times \mathbf{B} - \frac{1}{2\rho} \nabla \mathcal{E}, \quad (2)$$

$$\frac{\partial \mathbf{B}}{\partial t} = \nabla \times (\mathbf{u} \times \mathbf{B}), \quad (3)$$

$$\begin{aligned} \frac{\partial}{\partial t} \left( \frac{\rho u^2}{2} + \frac{P}{\gamma-1} + \frac{B^2}{8\pi} - \frac{\rho GM_\odot}{r} + \mathcal{E} \right) \\ = -\nabla \cdot \left[ \left( \frac{\rho u^2}{2} + \frac{\gamma P}{\gamma-1} - \frac{\rho GM_\odot}{r} \right) \mathbf{u} \right. \\ \left. + \frac{\mathbf{B}}{4\pi} \times (\mathbf{u} \times \mathbf{B}) + \left( \frac{3}{2} \mathbf{u} + \mathbf{V}_A \right) \mathcal{E} \right], \quad (4) \end{aligned}$$

$$\frac{\partial \mathcal{E}}{\partial t} + \nabla \cdot [(\mathbf{u} + \mathbf{V}_A) \mathcal{E}] + \frac{\mathcal{E}}{2} \nabla \cdot \mathbf{u} = -|\mathbf{u} + \mathbf{V}_A| \frac{\mathcal{E}}{L}, \quad (5)$$

where the dependent variables are mass density  $\rho$ , velocity  $\mathbf{u}$ , magnetic field  $\mathbf{B}$ , pressure  $P$ , and Alfvén wave energy density  $\mathcal{E}$  ( $= \langle \delta B^2 \rangle / 4\pi = \rho \langle \delta V^2 \rangle$ , where  $\langle \delta B^2 \rangle$  and  $\langle \delta V^2 \rangle$  are the mean square amplitudes of magnetic and velocity fluctuations). Other notations are the time  $t$ , the radial distance from the solar cen-

ter ( $r$ ), the polytropic index  $\gamma$ , the gravitational constant  $G$ , the solar mass  $M_\odot$ , a unit vector in the radial direction  $\hat{r}$ , and the velocity of outward propagating Alfvén waves ( $\mathbf{V}_A$ ) ( $\mathbf{V}_A = \mathbf{B}/(4\pi\rho)^{1/2}$  if  $B_r \geq 0$ , and  $\mathbf{V}_A = -\mathbf{B}/(4\pi\rho)^{1/2}$  if  $B_r < 0$ ).

Heat conduction processes in the solar wind are not well understood [Hollweg, 1992], and there is no general agreement as to what form the heat transport terms should take in the energy equation. Here we adopt an explicit formulation of the heat conduction using a polytropic approximation with a nonadiabatic value of  $\gamma < 5/3$ . Values of  $\gamma$  greater than  $\sim 1.10$  (we use  $\gamma = 1.12$  for the region  $1 \leq r \leq 20 R_\odot$ ) correspond to a slow wind and can be mathematically identified with a collisionless heat conduction flux of moderate intensity [Jacques, 1978]. This is admittedly a simplification, because the heat flux in the solar wind is primarily carried by the nonthermal tail of the electron distribution [see, e.g., Scime et al., 1994] and is more properly described by a kinetic formalism [Dorelli and Scudder, 1999]. In the lower corona the mean free path of particles is less than the temperature scale height, so that the thermal conduction can be approximated by the classical formula [Spitzer, 1962]. In the highly tenuous upper corona and solar wind (outside  $5\text{--}10 R_\odot$ ) the mean free path is comparable to or greater than the scale height (the continuum approach may still be applicable when waves and instabilities are taken into account), and a collisionless form for the heat conduction flux should be used (a recent generalization of the Spitzer-Härm heat conduction to Kappa electron distributions can be found in the work of Dorelli and Scudder [1999]). Success in obtaining the correct three-dimensional structure, speed, and density will provide important constraints on more detailed kinetic theories of heating and can provide realistic initial conditions for time-dependent studies of the evolution of turbulence in the solar wind [Goldstein et al., 1995, 1999]. Precisely how the energy balance in the corona is achieved, albeit of profound theoretical importance, is beyond the scope of this paper, which has the more limited focus of attempting to constrain some of the thermodynamic properties of the corona in such a way as to be consistent with Ulysses observations.

Use of the WKB approximation is justified by the analyses of Roberts [1989], Roberts et al. [1990], and Smith et al. [1995b] who showed that the observed evolution of intermediate- to large-scale interplanetary fluctuations agrees with WKB theory between 0.3 and 20 AU, notwithstanding the issue mentioned above that extrapolating the wave flux back to the Sun suggests that it is insufficient to accelerate high-velocity streams. For our purposes, neither the frequency spectrum nor the damping mechanism of such a wave population is important. Instead, we postulate the existence of waves with an energy density somewhat greater than that expected from the WKB extrapolations. If the large ve-

locity fluctuations observed in solar corona are Alfvénic and if Alfvén waves are important in accelerating the solar wind, then, to match the observed wave energy flux, the waves should damp between the coronal base and the distant wind. Spacecraft data outside  $60 R_\odot$  ( $\sim 0.3$  AU) show apparently no evidence of wave damping [Roberts, 1989; Roberts et al., 1990] except as a consequence of a turbulent cascade [Tu, 1987; Verma et al., 1995]. Also, Alfvén wave amplitudes are relatively small near the Sun, up to  $\sim 10\text{--}20 R_\odot$ , so it is likely that the waves are subject to little damping in this region [Hollweg, 1973; Esser et al., 1986, Tu, 1987]. Therefore our choices for the exponential damping length  $L$  assume that there is almost no damping ( $L = 80 R_\odot$ ) inside  $20 R_\odot$ , relatively large damping ( $L = 10 R_\odot$ ) between  $20 \leq r \leq 60 R_\odot$ , and no damping ( $L \rightarrow \infty$ ) beyond  $60 R_\odot$ , so that Alfvén waves at large heliocentric distances still have significant amplitudes.

We neglect solar rotation and all gradients in the azimuthal direction and assume that the velocity and magnetic field vectors possess components only in the radial and meridional directions. As the purpose of this work is to model globally the coronal structure in the region that extends from  $1 R_\odot$  to 5 AU, we reduce computational demands by dividing the computational domain into two regions: an inner region I ( $1\text{--}20 R_\odot$ ), where we search for a steady state solution by using a time relaxation method [Endler, 1971; Steinolfson et al., 1982; Washimi et al., 1987; Linker et al., 1990; Usmanov, 1993a, b, c; Wang et al., 1993; Mikić and Linker, 1996], and an outer region II ( $20 R_\odot\text{--}5$  AU), where the flow is assumed to be supersonic and super-Alfvénic and where a solution is obtained by a forward integration along the radius [Goldstein and Jokipii, 1977; Pizzo, 1982; Usmanov, 1993a, b, c]. Once a steady state solution in region I is obtained, a slice of the solution at the region I–II interface ( $20 R_\odot$ ) is used as a boundary condition to start integration throughout region II. We choose  $\gamma = 1.12$  in the near-Sun region I but use  $\gamma = 1.46$  (inferred from Helios observations by Totten et al. [1995]) in region II. These values of  $\gamma$  are characteristic of slow wind, while incorporation of Alfvén waves produces fast terminal velocities [cf. Alazraki and Couturier, 1971; Jacques, 1978].

### 3.1. Region I ( $1\text{--}20 R_\odot$ )

One difficulty in simulating the plasma-magnetic field interaction in the solar corona is that close to the solar surface, where radial gradients are large, the atmospheric expansion is subsonic, and hence the atmosphere is close to hydrostatic equilibrium. Consequently, the density decrease is approximately exponential. To handle this, we use the following substitutions in (1)–(5):  $\rho \rightarrow \rho\rho_0(r)$ ,  $\mathbf{u} \rightarrow \mathbf{u}u_0(r)$ ,  $\mathbf{B} \rightarrow \mathbf{B}B_0(r)$ ,  $P \rightarrow PP_0(r)$ , and  $\mathcal{E} \rightarrow \mathcal{E}\mathcal{E}_0(r)$ . We assume that  $\rho_0(r)$ ,  $u_0(r)$ ,  $P_0(r)$ , and  $\mathcal{E}_0(r)$  are solutions of (1)–(5) in a steady spherically symmetric situation, so that

$$\frac{d}{dr}(r^2 \rho_0 u_0) = 0, \quad (6)$$

$$u_0 \frac{du_0}{dr} + \frac{1}{\rho_0} \frac{d}{dr} \left( P_0 + \frac{\mathcal{E}_0}{2} \right) + \frac{GM_\odot}{r^2} = 0, \quad (7)$$

$$\frac{d}{dr} \frac{P_0}{\rho_0^\gamma} = \frac{(\gamma-1)(u_0 + V_{Ar}^0) \mathcal{E}_0}{u_0 \rho_0^\gamma L}, \quad (8)$$

$$\frac{d}{dr} \left[ \frac{r^2(u_0 + V_{Ar}^0)^2 \mathcal{E}_0}{V_{Ar}^0} \right] = - \frac{r^2(u_0 + V_{Ar}^0)^2 \mathcal{E}_0}{V_{Ar}^0 L}, \quad (9)$$

where  $V_{Ar}^0 = B_S(r_S/r)^2/(4\pi\rho_0)^{1/2}$  and  $B_S$  is the magnetic field strength at the coronal base  $r = r_S$ . This approach concentrates the gradients in the normalization functions while allowing the dependent variables to describe deviations from the initial flow. If we choose  $B_0(r) = B_S(r/r_S)^{-p}$ , then (1)–(5) can be rewritten in spherical coordinates  $(r, \theta)$  in the meridional plane as

$$\frac{1}{S_h} \frac{\partial \rho}{\partial t} + u_r \frac{\partial \rho}{\partial r} + \rho \frac{\partial u_r}{\partial r} + \frac{u_\theta}{r} \frac{\partial \rho}{\partial \theta} + \frac{\rho}{r} \frac{\partial u_\theta}{\partial \theta} + \frac{\rho u_\theta \cot \theta}{r} = 0, \quad (10)$$

$$\begin{aligned} \frac{1}{S_h} \frac{\partial u_r}{\partial t} + u_r \frac{\partial u_r}{\partial r} + \frac{u_\theta}{r} \frac{\partial u_r}{\partial \theta} - \frac{u_\theta^2}{r} &= - \frac{E_u}{\rho} \frac{\partial P}{\partial r} \\ &- \frac{E_w}{\rho} \frac{\partial \mathcal{E}}{\partial r} - \frac{B_\theta}{\rho M_A^2} \left[ \frac{\partial B_\theta}{\partial r} - \frac{1}{r} \frac{\partial B_r}{\partial \theta} + \frac{(1-p)B_\theta}{r} \right] \\ &+ (P/\rho - 1) \frac{1}{F_r r^2} + (P/\rho - u_r^2) \frac{K}{r} \\ &- \frac{E_w(P - \mathcal{E})}{\rho} \left[ \frac{(3M_A' + 1)(K + 2)}{2r(M_A' + 1)} + \frac{1}{L} \right], \end{aligned} \quad (11)$$

$$\begin{aligned} \frac{1}{S_h} \frac{\partial u_\theta}{\partial t} + u_r \frac{\partial u_\theta}{\partial r} + \frac{u_\theta}{r} \frac{\partial u_\theta}{\partial \theta} + \frac{u_r u_\theta (K + 1)}{r} &= \\ &= - \frac{E_u}{\rho r} \frac{\partial P}{\partial \theta} - \frac{E_w}{\rho r} \frac{\partial \mathcal{E}}{\partial \theta} \\ &+ \frac{B_r}{\rho M_A^2} \left[ \frac{\partial B_\theta}{\partial r} - \frac{1}{r} \frac{\partial B_r}{\partial \theta} + \frac{(1-p)B_\theta}{r} \right], \end{aligned} \quad (12)$$

$$\begin{aligned} \frac{1}{S_h} \frac{\partial B_r}{\partial t} &= \frac{B_\theta}{r} \frac{\partial u_r}{\partial \theta} - u_r \frac{\partial B_r}{\partial r} - \frac{u_\theta}{r} \frac{\partial B_r}{\partial \theta} \\ &- \frac{B_r}{r} \left[ (2-p)u_r + u_\theta \cot \theta + \frac{\partial u_\theta}{\partial \theta} \right], \end{aligned} \quad (13)$$

$$\begin{aligned} \frac{1}{S_h} \frac{\partial B_\theta}{\partial t} &= B_r \frac{\partial u_\theta}{\partial r} - u_r \frac{\partial B_\theta}{\partial r} - \frac{u_\theta}{r} \frac{\partial B_\theta}{\partial \theta} - B_\theta \frac{\partial u_r}{\partial r} \\ &+ \frac{1}{r} [u_\theta B_r (K - 1) - u_r B_\theta (K - p + 1) \\ &- u_\theta B_\theta \cot \theta], \end{aligned} \quad (14)$$

$$\begin{aligned} \frac{1}{S_h} \frac{\partial P}{\partial t} + \gamma P \left( \frac{\partial u_r}{\partial r} + \frac{1}{r} \frac{\partial u_\theta}{\partial \theta} + \frac{u_\theta \cot \theta}{r} \right) \\ + u_r \frac{\partial P}{\partial r} + \frac{u_\theta}{r} \frac{\partial P}{\partial \theta} &= \frac{2(\gamma-1)E_w}{E_u M_A' L} \\ &\times [M_A' |\mathbf{u} + \mathbf{V}_A| \mathcal{E} - (M_A' + 1)u_r P], \end{aligned} \quad (15)$$

$$\begin{aligned} \frac{1}{S_h} \frac{\partial \mathcal{E}}{\partial t} &= \frac{\mathcal{E}}{2\rho} \left( V_{Ar} \frac{\partial \rho}{\partial r} + \frac{V_{A\theta}}{r} \frac{\partial \rho}{\partial \theta} \right) - (u_r + V_{Ar}) \frac{\partial \mathcal{E}}{\partial r} \\ &- \frac{u_\theta + V_{A\theta}}{r} \frac{\partial \mathcal{E}}{\partial \theta} - \frac{3\mathcal{E}}{2} \left( \frac{\partial u_r}{\partial r} + \frac{1}{r} \frac{\partial u_\theta}{\partial \theta} \right) \\ &- \frac{\mathcal{E}}{r} \left[ \frac{3u_\theta \cot \theta}{2} + \frac{(u_r - M_A' V_{Ar})(K + 2)}{M_A' + 1} \right] \\ &+ \frac{\mathcal{E}}{L} (u_r + V_{Ar} - |\mathbf{u} + \mathbf{V}_A|), \end{aligned} \quad (16)$$

where the independent variables are  $t$ ,  $r$ , and  $\theta$ . The nondimensional functions are the Strouhal number  $S_h(r) = u_0 \tilde{T}/\tilde{L}$ , the Froude number  $F_r(r) = \tilde{L}u_0^2/GM_\odot$ , the Euler number  $E_u(r) = P_0/\rho_0 u_0^2$ , and the Alfvén Mach number  $M_A(r) = u_0(4\pi\rho_0)^{1/2}/B_0$ .  $\tilde{T}$  and  $\tilde{L}$  are characteristic values of time and length. Other nondimensional functions are defined as  $E_w(r) = \mathcal{E}_0/2\rho_0 u_0^2$ ,  $K(r) = (r/u_0)du_0/dr$ , and  $M_A' = (r/r_S)^{2-p} M_A$ . The normalized velocity of Alfvén waves is  $\mathbf{V}_A = (V_{Ar}, V_{A\theta}) = \mathbf{B}/\sqrt{\rho}M_A$  if  $B_r \geq 0$  and  $\mathbf{V}_A = -\mathbf{B}/\sqrt{\rho}M_A$  if  $B_r < 0$ . Note that the normalized and unnormalized equations differ only in terms that do not contain derivatives. To reduce further the number of mesh points along the radius, we use a logarithmic transformation of  $r$  to a new dimensionless coordinate  $r' = \ln(r/r_S)$ .

### 3.2. Region II (20–215 $R_\odot$ )

In the absence of a steady electric field in the solar corona, in a steady state the plasma should flow along the magnetic field lines, i.e.,  $\mathbf{u} \parallel \mathbf{B}$ , and one of the magnetic field components, for example,  $B_\theta$ , can be computed from the relation  $B_\theta = u_\theta B_r/u_r$  [Pizzo, 1982]. The steady state equations in conservation form can then be obtained from (1)–(5) by setting  $\partial/\partial t = 0$  and by using the divergence-free condition instead of the induction equation (3), so that

$$\frac{\partial}{\partial r}(r^2 \rho u_r) = - \frac{r}{\sin \theta} \frac{\partial}{\partial \theta}(\sin \theta \rho u_\theta), \quad (17)$$

$$\begin{aligned} \frac{\partial}{\partial r} \left[ r^2 \left( \rho u_r^2 + P + \frac{\mathcal{E}}{2} + \frac{B_\theta^2 - B_r^2}{8\pi} \right) \right] &= \\ &= - \frac{r}{\sin \theta} \frac{\partial}{\partial \theta} \left[ \sin \theta \left( \rho u_r u_\theta - \frac{B_r B_\theta}{4\pi} \right) \right] \\ &- r \rho \left( u_\theta^2 - \frac{GM_\odot}{r} + \frac{2P + \mathcal{E}}{\rho} + \frac{B_r^2}{4\pi\rho} \right), \end{aligned} \quad (18)$$

$$\begin{aligned} & \frac{\partial}{\partial r} \left[ r^3 \left( \rho u_r u_\theta - \frac{B_r B_\theta}{4\pi} \right) \right] \\ &= -r^2 \frac{\partial}{\partial \theta} \left( \rho u_\theta^2 + P + \frac{\mathcal{E}}{2} + \frac{B_r^2 - B_\theta^2}{8\pi} \right) \\ & - r^2 \cot \theta \left( \rho u_\theta^2 - \frac{B_\theta^2}{4\pi} \right), \end{aligned} \quad (19)$$

$$\frac{\partial}{\partial r} (r^2 B_r) = -\frac{r}{\sin \theta} \frac{\partial}{\partial \theta} (\sin \theta B_\theta), \quad (20)$$

$$\begin{aligned} & \frac{\partial}{\partial r} \left\{ r^2 \left[ u_r \left( \frac{\rho u^2}{2} + \frac{\gamma P}{\gamma-1} \right) + \left( \frac{3}{2} u_r + V_{Ar} \right) \mathcal{E} \right] \right\} \\ &= -\frac{r}{\sin \theta} \frac{\partial}{\partial \theta} \left\{ \sin \theta \left[ u_\theta \left( \frac{\rho u^2}{2} + \frac{\gamma P}{\gamma-1} \right) \right. \right. \\ & \left. \left. + \left( \frac{3}{2} u_\theta + V_{A\theta} \right) \mathcal{E} \right] \right\} - \rho u_r G M_\odot, \end{aligned} \quad (21)$$

$$\begin{aligned} & \frac{\partial}{\partial r} \left[ \frac{r^2 u_r (u + V_A)^2 \mathcal{E}}{u V_A} \right] = \\ & -\frac{r}{\sin \theta} \frac{\partial}{\partial \theta} \left[ \frac{\sin \theta u_\theta (u + V_A)^2 \mathcal{E}}{u V_A} \right] \\ & - \frac{r^2 (u + V_A)^2 \mathcal{E}}{V_A L}, \end{aligned} \quad (22)$$

where  $\mathbf{V}_A = (V_{Ar}, V_{A\theta}) = \mathbf{B}/(4\pi\rho)^{1/2}$  if  $B_r \geq 0$  and  $\mathbf{V}_A = -\mathbf{B}/(4\pi\rho)^{1/2}$  if  $B_r < 0$ ,  $V_A = (V_{Ar}^2 + V_{A\theta}^2)^{1/2}$ , and  $u = (u_r^2 + u_\theta^2)^{1/2}$ .

## 4. Initial State and Boundary Conditions

### 4.1. Initial Conditions

To start the relaxation process in region I, values of all dependent variables are assigned to each mesh point at  $t = 0$ . The initial distribution of flow parameters is given by a solution of the one-dimensional equations (6)–(9). Equations (6)–(9) can be reduced to the following single differential equation for the radial velocity:

$$\begin{aligned} & \frac{u_0^2 - c_{s0}^2 - u_{A0}^2}{u_0} \frac{du_0}{dr} = \frac{2(c_{s0}^2 + u_{A0}^2)}{r} - \frac{GM_\odot}{r^2} \\ & - \left[ \left( \frac{3}{2} + \frac{V_{Ar}^0}{u_0} \right) (\gamma - 1) - \frac{\gamma}{2} \right] \frac{\mathcal{E}_0}{\rho_0 L}, \end{aligned} \quad (23)$$

where

$$c_{s0}^2 = (\gamma - 1) \left[ \frac{F_T}{\Phi} - \frac{u_0^2}{2} + \frac{GM_\odot}{r} - \left( \frac{3}{2} + \frac{V_{Ar}^0}{u_0} \right) \frac{\mathcal{E}_0}{\rho_0} \right],$$

$$u_{A0}^2 = \frac{3u_0 + V_{Ar}^0}{4(u_0 + V_{Ar}^0)} \frac{\mathcal{E}_0}{\rho_0},$$

$$\mathcal{E}_0 = \mathcal{E}_{0S} \frac{V_{Ar}^0 r_S^2 (u_0^S + V_{Ar}^{0S})^2}{V_{Ar}^{0S} r^2 (u_0 + V_{Ar}^0)^2} \exp \left( -\frac{r - r_S}{L} \right),$$

$$\begin{aligned} F_T = \Phi \left[ \frac{(u_0^S)^2}{2} + \frac{\gamma}{\gamma - 1} \frac{2k_B T_S}{m_p} - \frac{GM_\odot}{r_S} \right] \\ + r_S^2 \left( \frac{3}{2} u_0^S + V_{Ar}^{0S} \right) \mathcal{E}_{0S}. \end{aligned}$$

$\Phi$  and  $F_T$  are the mass and the energy fluxes, respectively, per unit solid angle;  $u_0^S$ ,  $T_S$ ,  $\mathcal{E}_{0S}$ , and  $V_{Ar}^{0S}$  are the velocity, temperature, wave energy density, and Alfvén velocity at  $r = r_S$ ,  $k_B$  is the Boltzmann constant, and  $m_p$  is the proton mass. Specification of  $r_S$ ,  $T_S$ ,  $B_S$ ,  $\mathcal{E}_{0S}$ ,  $\Phi$ ,  $\gamma$ , and  $L$  would suffice to obtain a solution. The function  $u_0^S$  is chosen so that the solution passes through the critical point where both the right-hand side of (23) and the coefficient of  $du_0/dr$  are equal to zero (see Appendix A for details). We choose the following values:  $r_S = 1 R_\odot$ ,  $T_S = 1.8 \times 10^6$  K,  $\Phi = 3.4 \times 10^{11}$  g s<sup>−1</sup> sr<sup>−1</sup>,  $\gamma = 1.12$ , and  $L = 80 R_\odot$ . The parameters to be determined are  $B_S$  and  $\mathcal{E}_{0S}$ . We assume that the magnetic field in the initial state ( $t = 0$ ) is a dipole, i.e.,

$$B_r = B_d \left( \frac{r_S}{r} \right)^3 \cos \theta, \quad B_\theta = \frac{B_d}{2} \left( \frac{r_S}{r} \right)^3 \sin \theta,$$

where  $B_d = 18$  G is the magnetic field strength at the pole ( $\theta = 0^\circ$ ) on the initial level ( $r = r_S$ ). We assume that in the initial state the flow along each radial line can be described by the functions  $\rho_0$ ,  $u_0$ ,  $P_0$ , and  $\mathcal{E}_0$  as given by a solution of (6)–(9) with  $B_S = B_r(\theta)|_{r=r_S} = B_d \cos \theta$  and  $\mathcal{E}_{0S}|_{r=r_S} = \rho_{0S} \delta V_{0S}^2$ , where  $\rho_{0S} = \Phi/r_S^2 u_0^S$  is the density and  $\delta V_{0S} = < \delta V^2 >^{1/2}$  is the driven Alfvén wave amplitude at  $r = r_S$ . We assume further that  $\delta V_{0S}$  increases when the magnetic field configuration changes from a closed type (near  $\theta = 90^\circ$ ) to an open one (near  $\theta = 0$ ). To approximate this change, we choose the function  $\delta V_{0S} = \delta V_M \cos^{1/2} \theta$  with  $\delta V_M = 35$  km s<sup>−1</sup>. Figure 1 shows the radial dependence of  $\rho_0$ ,  $u_0$ ,  $P_0$ , and  $\mathcal{E}_0$ , from solving (6)–(9) along  $\theta = 0^\circ$  and  $\theta = 90^\circ$ . Setting  $\delta V_M = 0$  in (23) recovers the well-known result [Parker, 1963].

### 4.2. Boundary Conditions

To complete the formulation of the mixed initial boundary value problem in region I, we must specify the dependent variables at the inflow ( $1 R_\odot$ ) and outflow ( $20 R_\odot$ ) boundaries. It follows from the method of projected characteristics [Hu and Wu, 1984; Wang et al., 1982] that the number of dependent variables specified arbitrarily at a boundary must equal the number of incoming characteristics (projected on the radial direction) which start from the boundary and enter the computational domain. Other dependent variables must be determined from the differential equations (which are referred to as compatibility relations) along the outgo-

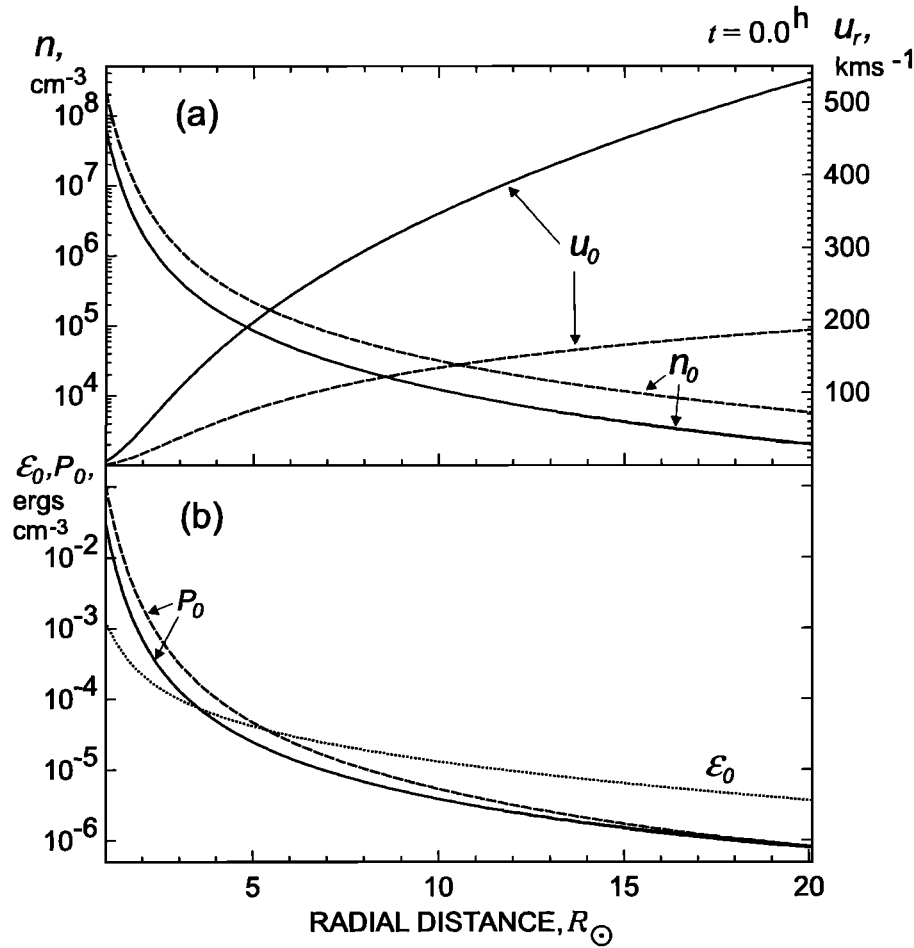


**Figure 1.** Radial dependence of the solutions of equations (6)–(9) along  $\theta = 0^\circ$  (solid lines) and  $\theta = 90^\circ$  (dashed lines): (a) radial velocity  $u_0$  and number density  $n_0$  and (b) pressure  $P_0$  and wave energy density  $\mathcal{E}_0$ .

ing characteristics (coming from the computational domain to the boundary). In our two-dimensional case the vector of dependent variables consists of seven elements and, at the inflow boundary where the flow is assumed to be subsonic and sub-Alfvénic, we have two outgoing characteristics and five incoming ones. Therefore the values of any two variables can be determined from the flow parameters near the boundary using the compatibility relations, while the other five may be prescribed at our discretion. The present model employs a simple linear extrapolation procedure, which works well as a substitution for the full compatibility relations [Nakagawa and Steinolfson, 1976; Steinolfson et al., 1982].

Two variables we determine from extrapolation at  $1 R_\odot$  are, first, the tangential magnetic field component  $B_\theta$  and, second, either  $u_r$  or  $P$ . We solve for  $u_r$  so long as  $u_r > 0$  at the boundary; however, when its extrapolated value goes negative,  $u_r$  is fixed to zero and  $P$  is then solved for ( $P$  initially is fixed to its initial value so long as  $u_r > 0$ ). The variables  $u_\theta$  and  $\rho$  are computed from the relations  $u_\theta = u_r B_\theta / B_r$  and  $P / \rho^\gamma = \text{const}$ , respectively.  $\mathcal{E}$  is fixed to the initial value at the points

where  $u_r > 0$  and is set to zero where  $u_r = 0$ . We set  $\mathcal{E} = 0$  inside the streamer to avoid its “evaporation” due to finite dissipation. Finally,  $B_r$  is computed from the divergence-free condition.

The outer boundary of region I is a computational rather than a physical boundary, and we choose its radial position ( $20 R_\odot$ ) such that the flow at the boundary is supersonic and super-Alfvénic. Consequently, disturbances cannot propagate upstream into the computational domain, and all the characteristics projected on the radial direction are outgoing, which enables us to extrapolate all dependent variables at the boundary.

## 5. Simulation Results

### 5.1. Region I

The computation in region I starts from a radial Parker-type flow with Alfvén waves in a dipole magnetic field (section 4.1) as illustrated in Figure 2a, which shows a map of radial velocity magnitudes with the magnetic field lines superimposed (the lighter the shading, the higher the velocity). The field lines are traced



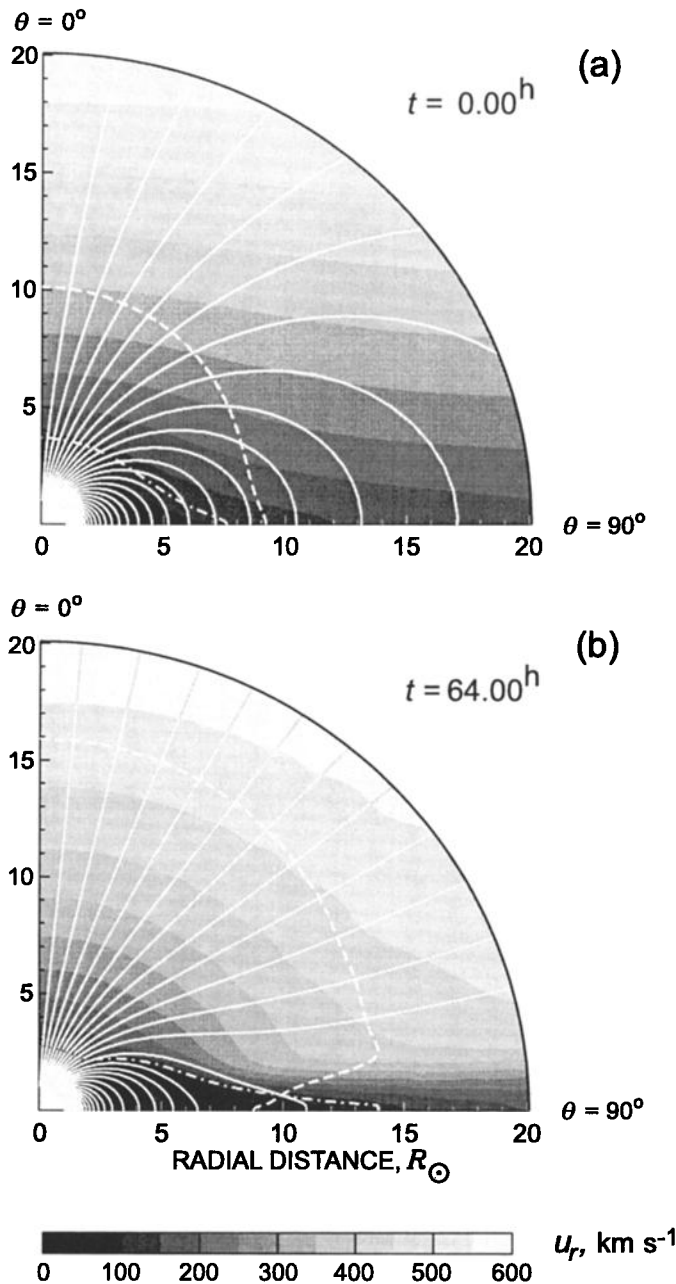


**Figure 2.** The magnetic field configuration in region I superimposed on a map of radial flow velocities (a) in the initial state and (b) after 64 hours of relaxation. The Alfvén curve (where the radial flow velocity is equal to the Alfvén velocity computed for the total magnetic field) is shown by the dashed line, and the sonic curve (where the radial velocity is equal to the sound velocity) is shown by the dash-dotted line.

from  $r = 1 R_{\odot}$  with the spacing of  $2^{\circ}$  between the pole at  $\theta = 0^{\circ}$  and the equator ( $\theta = 90^{\circ}$ ). After 64 hours of relaxation time (Figure 2b) a closed field region persists near the equator; the flow velocity is high in the open polar field region but decreases toward the equator above the region of closed magnetic field. Also plotted are the Alfvén curves where the flow velocity equals

the Alfvén velocity (calculated from the total magnetic field) and the sonic curves where the flow speed equals the sound speed. The transition to a super-Alfvénic regime occurs at  $\sim 14\text{--}16 R_{\odot}$ , except for a narrow band of slow velocities near the equator where the Alfvén curve dives inward to  $\sim 9 R_{\odot}$ . In contrast, the fast flow becomes supersonic much closer to the Sun, at  $\sim 3 R_{\odot}$ , while in the slow wind the sonic curve extends out to  $\sim 14 R_{\odot}$ .

In the outflow region,  $u_r$  is roughly uniform ( $\sim 20 \text{ km s}^{-1}$ ), and  $n$  is lower ( $6 \times 10^7 \text{ cm}^{-3}$ ) than in the nearby stagnation region ( $n \sim 10^8 \text{ cm}^{-3}$ ). In the outflow region the mass flux density is  $\sim 1.3 \times 10^{14} \text{ particles cm}^{-2} \text{ s}^{-1}$ , so that the Sun's mass loss is  $\sim 1.7 \times 10^{12} \text{ g s}^{-1}$ . The wave energy density  $\mathcal{E}$  peaks at the pole ( $\sim 1.3 \times 10^{-3} \text{ ergs cm}^{-3}$ ) and differs from zero only in the outflow region. The wave energy influx  $F_A = (3u_r/2 + V_{Ar})\mathcal{E}$  and the rms magnetic field amplitude of Alfvén waves,  $\delta B = (4\pi\mathcal{E})^{1/2}$ , vary similarly from  $6 \times 10^5 \text{ ergs cm}^{-2} \text{ s}^{-1}$  and 0.1 G, respectively, at the pole, to zero toward the equator. Recall that the amplitude of the Alfvén wave velocity fluctuations peaks at the pole where  $\delta V_M = 35 \text{ km s}^{-1}$ . This value is near the upper limit of nonthermal velocity amplitudes inferred from the line broadening in the near-Sun region by Hassler *et al.* [1990]. Because of the relaxation process,  $B_r$  and  $B_{\theta}$  on the boundary undergo only small changes and therefore approach a dipole-like distribution. Although a polar field strength of 18 G may seem high in comparison with the few gauss widely used in coronal modeling and with the intensity of the dipole component inferred from photospheric magnetic field measurements at the Wilcox Solar Observatory (WSO) at the time of the Ulysses fast latitude scan, uncertainties in interpreting the line-of-sight WSO data and in computing the magnetic field components, especially in the polar regions [Zhao and Hoeksema, 1995b; Wang and Sheeley, 1995], leave room for a wide range of the field strengths. Field magnitudes as high as 16 G [Wang and Sheeley, 1995], 20 G [Suess *et al.*, 1977], and even 30 G [Pneuman *et al.*, 1978] have been inferred from observations of polar coronal holes at epochs near solar minimum.

## 5.2. Velocity Structure

Contour plots of the radial and meridional velocities are shown in Figure 3 at  $t = 64.0$  hours. The flow stagnates near the equator (in Figure 3 the stagnation region is bounded with the zero contour line and is lightly shaded). The stagnation region extends from the inflow boundary at  $1 R_{\odot}$  (where it occupies the colatitudes up to  $\theta \sim 30^{\circ}$ ) out to  $\sim 7 R_{\odot}$  in the form of a torus with a sharp equatorial edge. It is clear from comparison with Figure 2b that the stagnation region matches the closed field region. Although we solve the ideal MHD equations, some numerical diffusion is present in addition to the artificial diffusion introduced by the Lapidus

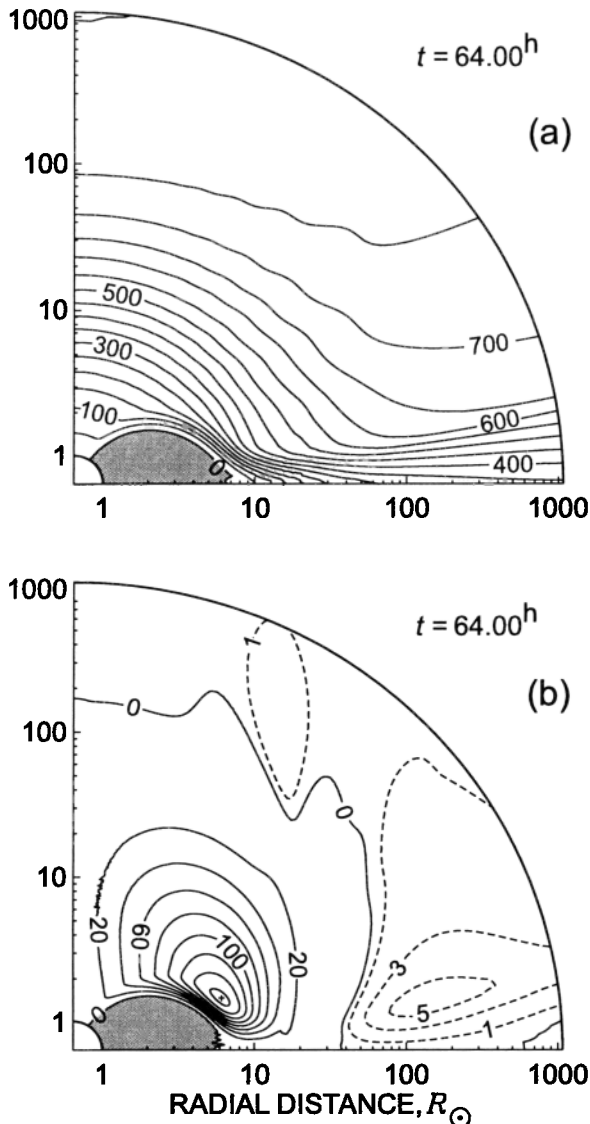


**Figure 3.** Contour maps of (a) radial velocities and (b) meridional velocities. Velocities are at radial distances from  $1 R_{\odot}$  to 5 AU. The equatorward (poleward) meridional velocities are shown by solid (dashed) lines.

method. This weak diffusion affects the solution primarily where gradients are large, in particular, in the vicinity of the equatorial current sheet. The field line that intersects the equator near  $11 R_{\odot}$  well above the streamer is apparently a result of this diffusion.

Except for a band above the stagnation region, the flow is only slightly dependent on latitude and accelerates up to velocities of  $\geq 700 \text{ km s}^{-1}$  along most of the outflow boundary at 5 AU. The coronal plasma flows around the stagnation region, with the highest transverse velocities appearing near the top of the region (Figure 3b, the peak value of  $u_{\theta}$  is  $166 \text{ km s}^{-1}$ ). The flow near the Sun is therefore highly nonradial, and both fast and slow winds originate in the region  $\theta \lesssim 30^{\circ}$  on the solar surface (see also Figure 4b). Thus the coronal

holes occupy the polar regions down to  $\theta \sim 30^{\circ}$  and cover only a small fraction ( $\sim 13\%$ ) of the solar surface. This agrees with observations of coronal holes at the time of Ulysses fast latitude traversal [Gosling *et al.*, 1995; Roberts and Goldstein, 1998].

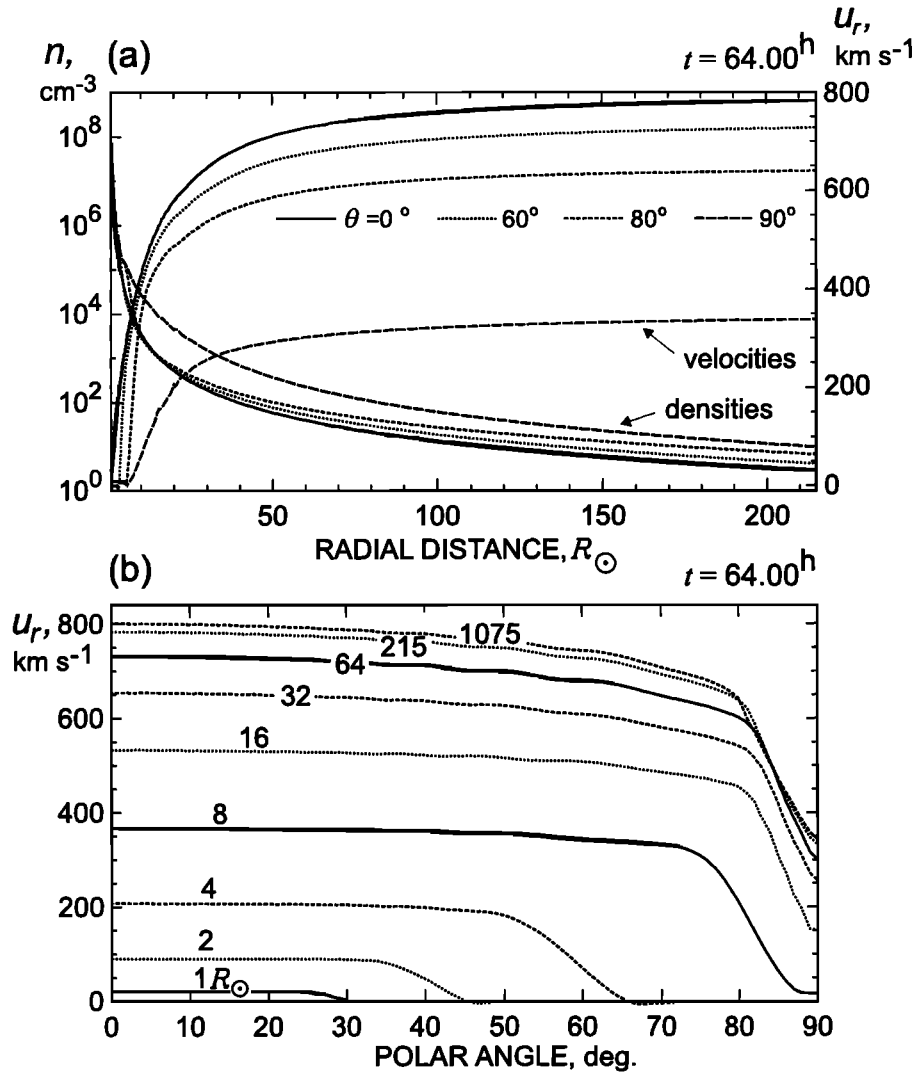
### 5.3. Plasma and Velocity Structure

Figure 4a shows the radial variations in plasma density and radial velocity from  $1 R_{\odot}$  to 1 AU versus heliocentric distance at various latitudes. The wind is fast along the  $\theta = 0^{\circ}$  and  $\theta = 60^{\circ}$  curves. At  $\theta = 80^{\circ}$  there is a transition to slow wind ( $\theta = 90^{\circ}$ ). The flow accelerates mainly in the near-Sun region ( $r \lesssim 30\text{--}40 R_{\odot}$ ), and the acceleration is greatest at the pole ( $u_r \sim 300 \text{ km s}^{-1}$  at  $r = 6 R_{\odot}$ ) where the velocity reaches  $\sim 650 \text{ km s}^{-1}$  by  $30 R_{\odot}$ . Along the equator the flow that has passed near the stagnation region accelerates more gradually, and  $u_r$  is only  $\sim 250 \text{ km s}^{-1}$  at  $30 R_{\odot}$ . The difference in velocity between the pole and equator is therefore  $\sim 400 \text{ km s}^{-1}$  at  $30 R_{\odot}$  and remains essentially constant for larger  $r$ .

The latitudinal variation of  $u_r$  at a number of distances between  $1 R_{\odot}$  and 5 AU is plotted in Figure 4b. At all distances the velocity varies only slightly across the flow except for a relatively narrow area around the stagnation region and along the helioequator. Meanwhile, some increase in the poleward gradient is noticeable with increasing heliocentric distance. Figure 4b allows one to see clearly the latitudinal extent of the stagnation region at 1, 2, and 4  $R_{\odot}$ , which reaches polar angles  $30^{\circ}$ ,  $45^{\circ}$ , and  $65^{\circ}$ , respectively. Note that the extent of the stagnation region at  $2 R_{\odot}$  agrees quite well with the estimated average width of the streamer belt at  $1.74 R_{\odot}$  inferred from Mauna Loa observations [Gosling *et al.*, 1995]. At 1 AU the flow velocity nearly approaches its asymptotic value: evident from the small difference between the velocity variation at 1 AU ( $787 \text{ km s}^{-1}$  at the pole and  $381 \text{ km s}^{-1}$  near the equator) and at 5 AU ( $820$  and  $426 \text{ km s}^{-1}$ ).

### 5.4. Magnetic Field and Plasma at 1 AU

In Figure 5 we plot the latitudinal variations of magnetic field and plasma parameters at 1 AU. Figure 5a shows  $B_r$  and the normalized electric current density  $(\nabla \times \mathbf{B})_{\phi}$ . At  $r = 215 R_{\odot}$ ,  $B_r \sim 3.2 \text{ nT}$  at the pole, increasing slowly with  $\theta$  up to  $\sim 4 \text{ nT}$  at  $\theta = 80^{\circ}$ , in qualitative agreement with the work of Smith *et al.* [2000]. It then drops steeply to zero toward the HCS. This behavior differs markedly from that at  $1 R_{\odot}$  where  $B_r$  decreased monotonically from pole to equator. It is clear from comparison with Figure 4b that the region  $0^{\circ}\text{--}80^{\circ}$  corresponds to the fast solar wind and that the region of strong gradient of  $B_r$  corresponds to intermediate and slow wind. The region of strong magnetic field gradient coincides with the region of strong electric currents. The currents are concentrated near the equator in a relatively thin current sheet with the current density



**Figure 4.** (a) Radial velocity and density versus distance at  $\theta = 0^\circ$ ,  $60^\circ$ ,  $80^\circ$ , and  $90^\circ$ . (b) Radial velocity versus polar angle at radial distances from  $1 R_\odot$  to 5 AU.

peaking near  $\theta = 90^\circ$ , where the gradient of  $B_r$  is the largest.

Figure 5b shows computed variations of wave energy density  $\mathcal{E}$ , Alfvén wave velocity amplitude  $\delta V$ , and thermal pressure  $P$ , versus latitude at  $215 R_\odot$ . The value of  $\mathcal{E}$  varies similarly to  $B_r$  and inversely to  $P$ , which is nearly an order of magnitude higher than  $\mathcal{E}$  and increases toward the equator. Unlike  $\mathcal{E}$ , which is weakly dependent on latitude in the fast wind ( $0^\circ$ – $80^\circ$ ),  $\delta V = (\mathcal{E}/\rho)^{1/2}$  reveals a modest poleward gradient that results from the decrease in plasma density toward the pole.

### 5.5. The Effect of Alfvén Waves

Figure 6 shows by solid lines the computed variations of  $\delta V$  and  $\delta B$  and of the ratio  $\delta B/B$  against heliocentric distance in the region from  $1 R_\odot$  to 1 AU along the polar axis ( $\theta = 0^\circ$ ). While  $\delta B$  decreases monotonically with  $r$ ,  $\delta V$  increases as  $\rho^{-1/4}$  in the near-Sun re-

gion (this follows from conservation of the wave energy flux  $F_A$  provided that  $V_A \gg u_r$ ), reaches its maximum of  $\sim 250$  km s<sup>-1</sup> at  $r \sim 16 R_\odot$  (where  $V_A \approx u_r$ ; see Figure 2), and decreases in the region outward (where  $V_A < u_r$ ) to  $\sim 15$  km s<sup>-1</sup> at 1 AU. Because of the assumed wave damping, the ratio  $\delta B/B$  is  $\leq 1$ , at all distances (in agreement with the empirical relation  $\delta B/B \lesssim 1$  which is characteristic of the distant solar wind [e.g., Belcher and Davis, 1971; Matthaeus and Goldstein, 1982]), increasing with  $r$  if  $r < 20 R_\odot$ , then decreasing in the region 20–60  $R_\odot$  (where the damping length is set to  $L = 10 R_\odot$ ), and increasing again outside 60  $R_\odot$  (where there is no damping).

To elucidate the effect of wave damping on the overall flow and magnetic field structure, we repeated the calculations in region II, first assuming that  $L = 80 R_\odot$  throughout the region (the dashed curves in Figure 6) and, second, assuming that  $L = 0.28r^{5/4}$  (where  $r$  and  $L$  are given in solar radii). In the latter case,  $L$  in-

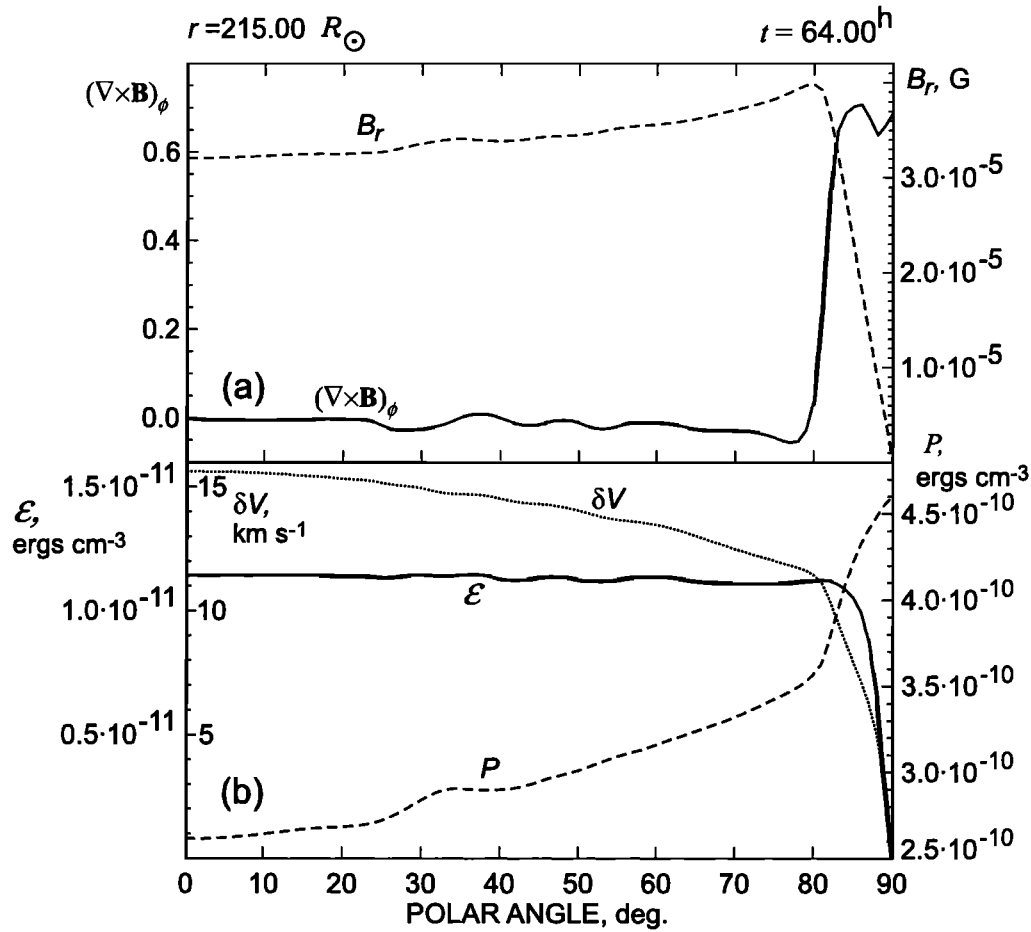


**Figure 5.** The polar angle variations at  $r = 215 R_{\odot}$  of (a) the radial magnetic field  $B_r$  and the electric current density  $(\nabla \times \mathbf{B})_{\phi}$  and (b) the thermal pressure  $P$ , the driven amplitude  $\delta V$ , and energy density  $\mathcal{E}$  of Alfvén waves.

creases from  $L = 12 R_{\odot}$  at  $r = 20 R_{\odot}$  to  $L = 230 R_{\odot}$  at  $r = 1 \text{ AU}$  (the dotted curves in Figure 6), which leads to the radially independent distribution of  $\delta B/B$  that is characteristic for models with a constant level of saturation [Hollweg, 1973]. However, Helios 2 observations indicate that such models are not consistent with observations [Roberts, 1989]. We found that the velocity, density, and magnetic field behave similarly for all three choices for the dependence of  $L$  on  $r$ ; however,  $\mathcal{E}$  and  $T$  differ, indicating that our calculations are insensitive to the details of how and where wave damping occurs (the differences in solar wind temperature at 1 AU in the three cases are  $\leq 6\%$ ).

### 5.6. A Solution Without Waves

To illustrate the importance of Alfvén waves in the model, we repeated the computation with  $\delta V_{0M} = 0$  to exclude all wave effects. The results are shown in Figures 7–9 in the same format as that in Figures 2–4. Now the initial state for hydrodynamic parameters is the Parker wind solution [Parker, 1963]. A comparison of Figures 2–4 and 7–9 shows that the topology of solution is very similar, i.e., a closed field region (where

plasma motions are impeded) embedded within open flux tubes where plasma streams freely outward. In both cases the flow structure exhibits a roughly homogeneous high-velocity stream with a more or less abrupt transition to lower velocities. However, quantitatively, the results differ markedly. First, without waves the velocities are low with peak values of 220 and 280  $\text{km s}^{-1}$  at 20 and 215  $R_{\odot}$ , respectively, compared with 480 and 615  $\text{km s}^{-1}$  when waves are included. Second, the density is very high ( $\geq 16 \text{ cm}^{-3}$ ) at 1 AU. These results are typical for solar wind models that do not include additional sources of acceleration for the solar wind flow [Hundhausen, 1972]. In addition, variations in velocity are more prominent in the case with waves. The amplitude of variations in  $u_r$  at 215  $R_{\odot}$  is  $\sim 400 \text{ km s}^{-1}$  with Alfvén waves (Figure 4b) and only  $\sim 60 \text{ km s}^{-1}$  without waves (Figure 9b).

## 6. Comparison With Ulysses Observations

Figure 10 plots against heliographic latitude the daily averages of radial magnetic field, radial velocity, number density, and plasma temperature as observed by

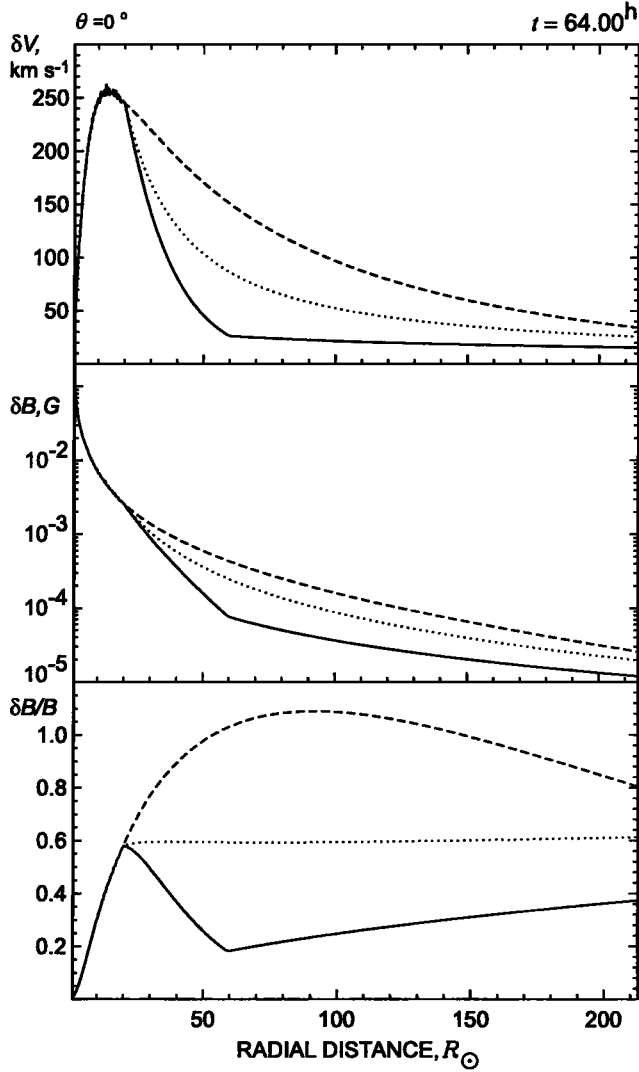


**Figure 6.** Velocity and magnetic field amplitudes of Alfvén waves ( $\delta V$  and  $\delta B$ ) and the ratio  $\delta B/B$  versus distance (solid lines). Dashed and dotted lines show variations in the models with  $L = 80 R_{\odot}$  throughout region II and with  $L = 0.28r^{5/4}$  simulating the damping with a constant saturation level.

Ulysses for the period from September 13, 1994, to July 31, 1995, covering  $-80.2^{\circ}$  to  $+80.2^{\circ}$  in latitude and 1.3–2.3 AU in heliocentric distance. Following Forsyth *et al.* [1996] and Phillips *et al.* [1995], we scaled the radial magnetic field intensity and number density to 1 AU assuming an  $r^{-2}$  falloff for both parameters. The observed plasma temperature has been normalized to 1 AU assuming an  $r^{-2(\gamma-1)}$  variation with  $\gamma = 1.46$ .

Two model curves are superimposed on each plot of Ulysses data in Figure 10. The dashed line (curve 1) is the prediction of the present model, extended symmetrically across the helioequator to the Southern Hemisphere. The model dotted line (curve 2) is the same solution but constructed separately for the Northern and Southern hemispheres merely by shifting the model

curve 1 by  $15^{\circ}$  north and south, respectively. Our motivation for producing the curve 2 was as follows: While the heliospheric structure was more or less axisymmetric in 1994–1995, the actual heliospheric current sheet deviated somewhat from the helioequatorial plane, forming a four-sector structure [Smith *et al.*, 1995a; Erdős and Balogh, 1998]. To calculate this effect, one really needs a three-dimensional model; however, averaging the deviation over longitude effectively broadens the band of slower velocities around the equator. Thus the model curve 2 is an attempt to account for the effect of HCS warping within the two-dimensional formulation.

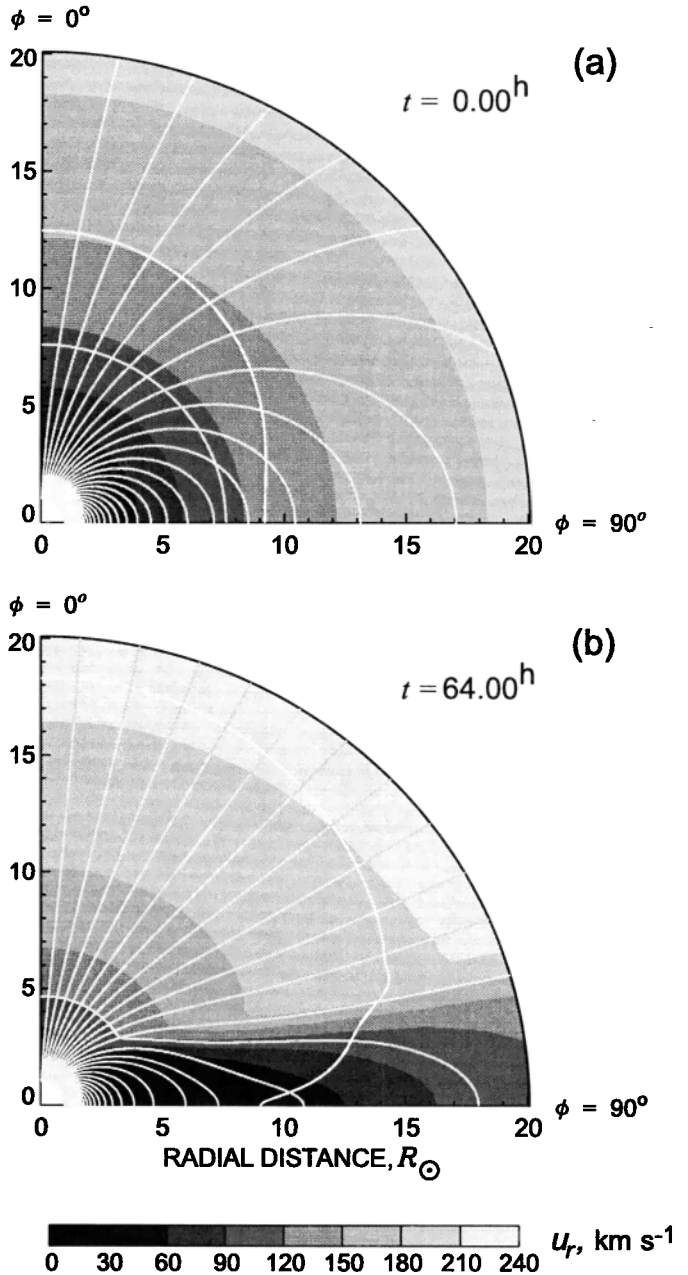


**Figure 7.** The same as in Figure 2 but for the model without Alfvén wave flux.

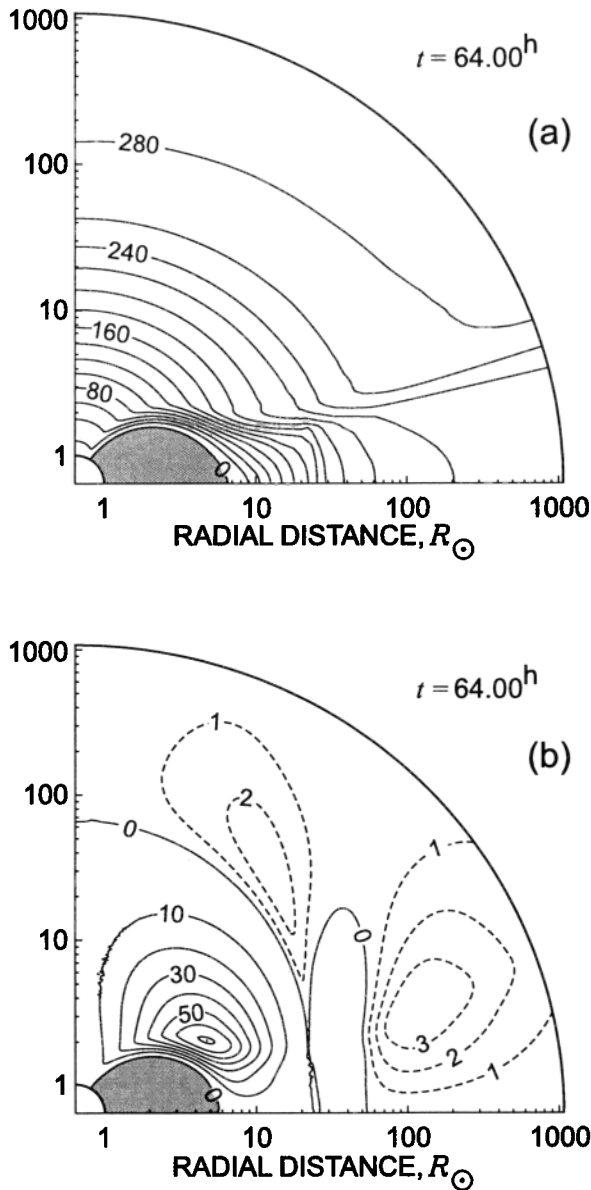


**Figure 8.** The same as in Figure 3 but for the model without Alfvén wave flux.

It is evident from Figure 10 that there is rough agreement between the computed and observed curves in each plot, especially for the model curve 2. Both magnitude and latitude variations of computed  $B_r$ ,  $u_r$ ,  $n$ , and  $T$  are similar to those in the Ulysses data. The bimodal structure of the solar wind (a combination of fast, uniform, unipolar, and tenuous polar flows, with a slow and relatively dense equatorial wind of alternating magnetic polarity) and even the width of the equatorial band and the sharpness of velocity transitions are fairly well reproduced by the model curve 2. The computed variations are, however, quite smooth, while the observed parameters undergo rapid changes which are particularly striking in the region around the equator. The changes can be attributed partly to transients such as coronal mass ejections and to other azimuthal asym-

metries of the near-equatorial region that are not included in the models.

An unexpected feature of Ulysses magnetic field measurements was the absence of a significant gradient of  $B_r$  with respect to heliolatitude in fast polar flows [Smith and Balogh, 1995; Forsyth et al., 1996; Smith et al., 1995c]. Figures 5a and 10 show that this phenomenon is reproduced in our simulation. To gain greater insight into the way a dipole magnetic field near the Sun is transformed into a constant magnitude one at large distances, we show in Figure 11 the computed evolution of latitudinal profiles of  $B_r$  with heliocentric distance from  $4 R_\odot$  to 5 AU. To be more specific, the dipolar gradient of  $B_r$  near the Sun does not vanish at larger distances; rather, it is redistributed along latitude, relaxing around the pole and becoming concentrated near the equator. This transformation begins at  $r > 4 R_\odot$  and is essentially complete by  $24 R_\odot$ . Note that for  $r > 24 R_\odot$  a slight equatorward gradient in  $B_r$  is established that increases gradually with heliocentric distance.

The mechanism underlying the latitudinal variation of the dipolar gradient of  $B_r$  can be understood from Figure 12a, which shows the computed radial variation of  $P$ ,  $\mathcal{E}$ , and  $\beta = 8\pi P/B^2$  along the polar axis ( $\theta = 0^\circ$ ). Both near  $1 R_\odot$  and (owing to assumed wave damping) at  $r \gtrsim 30 R_\odot$ ,  $P$  dominates  $\mathcal{E}$ . However, between 10 and  $30 R_\odot$ ,  $\mathcal{E}$  and also  $\nabla \mathcal{E}$  far exceed  $P$  and  $\nabla P$ , respectively. Therefore, in this region,  $\nabla \mathcal{E}$  is the main acceleration factor and together with the gradient of magnetic pressure is the most important component of the transverse pressure balance. To emphasize the role of the wave energy density, we computed, in addition to  $\beta$ , the parameter  $\beta_T = 8\pi(P + \mathcal{E})/B^2$  in which  $P$  is replaced by the sum of  $P$  and  $\mathcal{E}$ . Clearly,  $\beta_T$  approaches  $\beta$  both at  $r = 1$  and  $r > 60 R_\odot$  while  $\beta_T$  differs markedly from  $\beta$  where  $\mathcal{E}$  dominates  $P$ . Near the coronal base,  $\beta_T$  increases more rapidly than  $\beta$  and exceeds unity for  $r > 24 R_\odot$ , while  $\beta$  becomes greater than unity only for  $r > 50 R_\odot$ . Thus the transformation of the dipole field into a uniform structure occurs in the region of  $\beta_T \leq 1$  ( $r \leq 24 R_\odot$ ) and, following Suess et al. [1977] and Suess and Smith [1996], can be interpreted as the relaxation of meridional gradients in field strength due to dominance of the transverse magnetic pressure gradient force.

The equatorward gradient that appears in the region  $\beta_T > 1$  ( $r > 24 R_\odot$ ) is a consequence of the equatorward gradient in  $P$  that leads to a latitudinal redistribution of magnetic flux in the region where magnetic forces are negligible [Suess et al., 1977; Suess et al., 1996; Smith et al., 2000]. The meridional redistribution of magnetic flux is produced by meridional flows which are directed (see Figure 3b) equatorward in the region  $r \leq 24 R_\odot$  ( $\beta_T < 1$ ) and poleward in the region  $r \geq 24 R_\odot$  ( $\beta_T > 1$ ). Figure 12b shows the latitudinal distributions of  $\beta_T$  at a number of heliocentric distances ranging from  $1 R_\odot$  to 5 AU. Except for the slower-

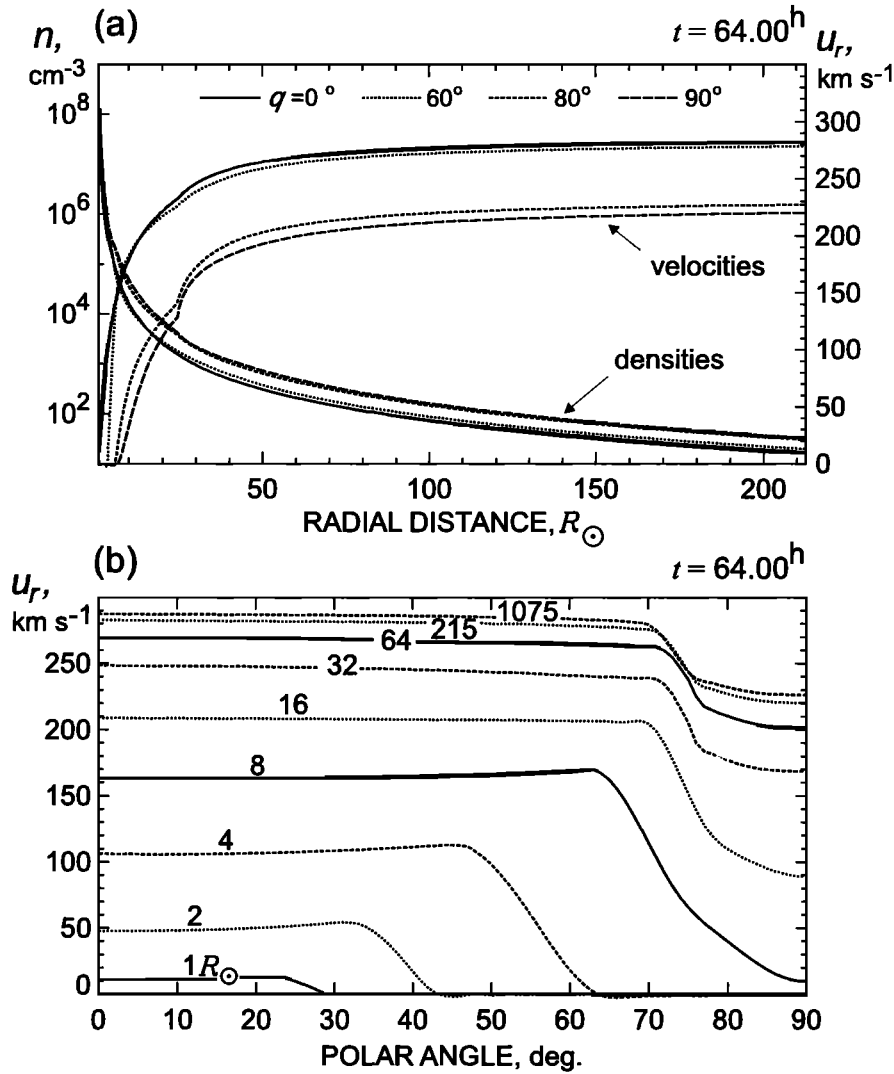


Figure 9. The same as in Figure 4 but for the model without Alfvén wave flux.

velocity equatorial band,  $\beta_T$  exhibits a weak decrease with latitude if  $\beta_T < 1$  and almost no latitude dependence in the region where  $\beta_T > 1$ . It follows that in the fast wind the magnetic pressure variation becomes more and more similar to that of  $P + \mathcal{E}$  as the heliocentric distance increases. In the distant wind, where  $\beta_T \gg 1$  and  $\mathcal{E}$  is negligible in comparison to  $P$ , the variation of magnetic pressure follows the thermal pressure.

As in the radial direction, the force balance along latitude is dynamic. Estimation of terms in (19) shows that in the fast distant wind the thermal pressure gradient is dominant, the thermal pressure and the radial magnetic field are both equatorward, and (19) is reduced to

$$\rho u_r \frac{\partial(r u_\theta)}{\partial \theta} \approx - \frac{\partial}{\partial \theta} \left( p + \frac{B_r^2}{8\pi} \right).$$

This means that plasma is flowing in the latitudinal direction, and this motion cannot be neglected in the meridional force balance.

The computed latitudinal variations of the areal expansion factor  $f_s$  between  $1 R_\odot$  and several heliocentric distances are shown in Figure 13. Again, with the exception of the equatorial band where  $f_s$  is very high, its variation is different in regions  $\beta_T < 1$  ( $r < 24 R_\odot$ ) and  $\beta_T > 1$  ( $r > 24 R_\odot$ ). If  $\beta_T < 1$ ,  $f_s$  increases monotonically from the pole to the equator, and, conversely, it decreases up to the equatorial band in the region with  $\beta_T > 1$ . Thus the latitudinal variations of  $f_s$  are also determined by two dominant dynamical processes in the expanding corona: (1) the primary meridional relaxation and formation of a flat meridional profile of all the flow and magnetic field parameters (outside the equatorial band) in the region where magnetic forces dominate the thermal and wave gradient forces (this occurs just where  $\beta_T \approx 1$ ) and (2) the secondary meridional redistribution due to the poleward thermal pressure gradient that formed as a result of the primary process. Consequences of the second process are the poleward gradient in  $u_r$  and the equatorward one in  $B_r$ , which develop in the fast distant wind.

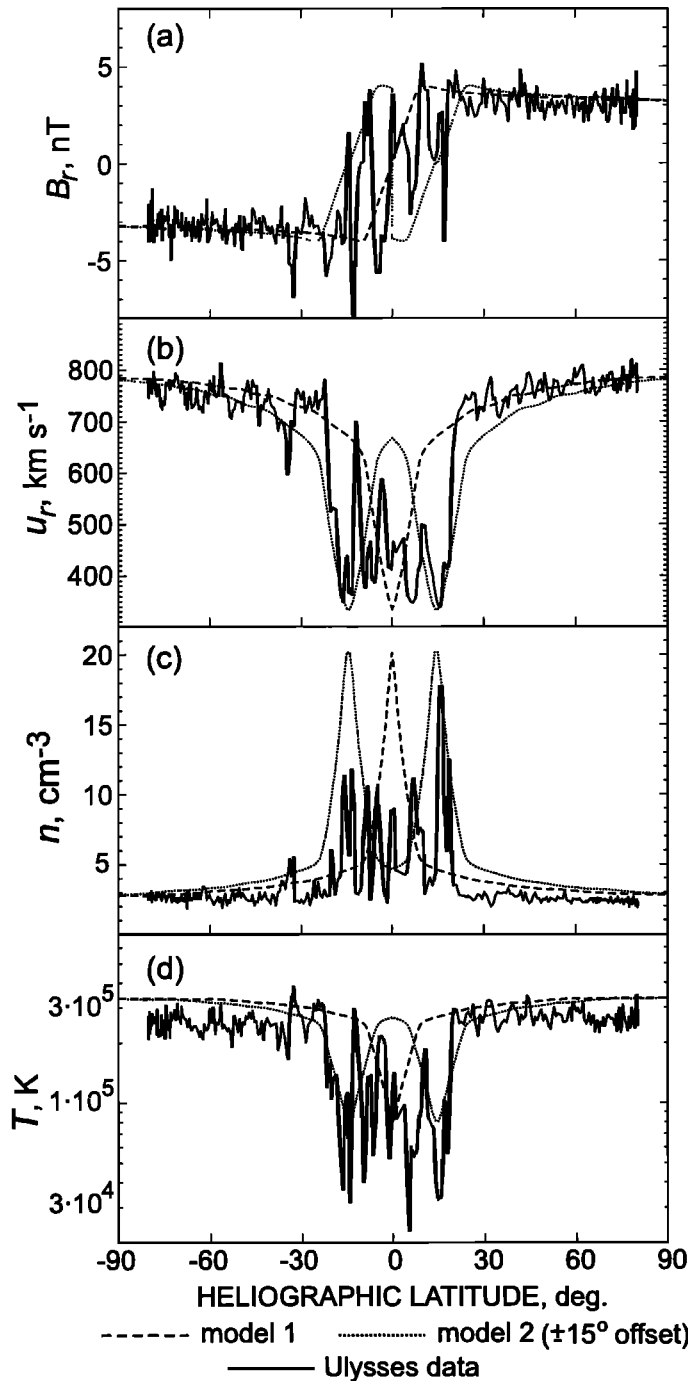


**Figure 10.** Daily averages of (a) radial magnetic field, (b) radial velocity, (c) number density, and (d) plasma temperature observed by Ulysses (solid lines). Plots are versus heliographic latitude and compared to latitude profiles computed in the present paper. The model curves are shown with dashed and dotted lines. The radial magnetic field, number density, and plasma temperature measured by Ulysses are normalized to 1 AU.

## 7. Conclusions

This paper represents an attempt to model quantitatively the physical properties of solar corona and solar wind on a global scale at the time of the Ulysses fast pole-to-pole scan in 1994-1995. We have developed an

axisymmetric self-consistent model of a steady coronal outflow with a balance of stresses between adjacent flow tubes. This model is based on a solution of the single-fluid ideal MHD equations in the region extending from the coronal base at  $1 R_\odot$  out to 5 AU. We assume that a large energy flux of Alfvén waves originates at the Sun in magnetically open polar regions. Consequently, the gradient of wave energy density plays a decisive role in accelerating the solar wind flow. The temperature of an outward flowing volume element of the solar wind represents a balance between adiabatic expansion with an implicit heating in the near-Sun region attributed to thermal conductivity, which is expressed by a non-adiabatic value of the polytropic index, and additional heating due to the damping of Alfvén waves.

The boundary conditions are specified at  $1 R_\odot$  and a steady state solution is obtained for a dipole surface magnetic field on the Sun and for an assumed Alfvén wave energy from the Sun into the open field regions.

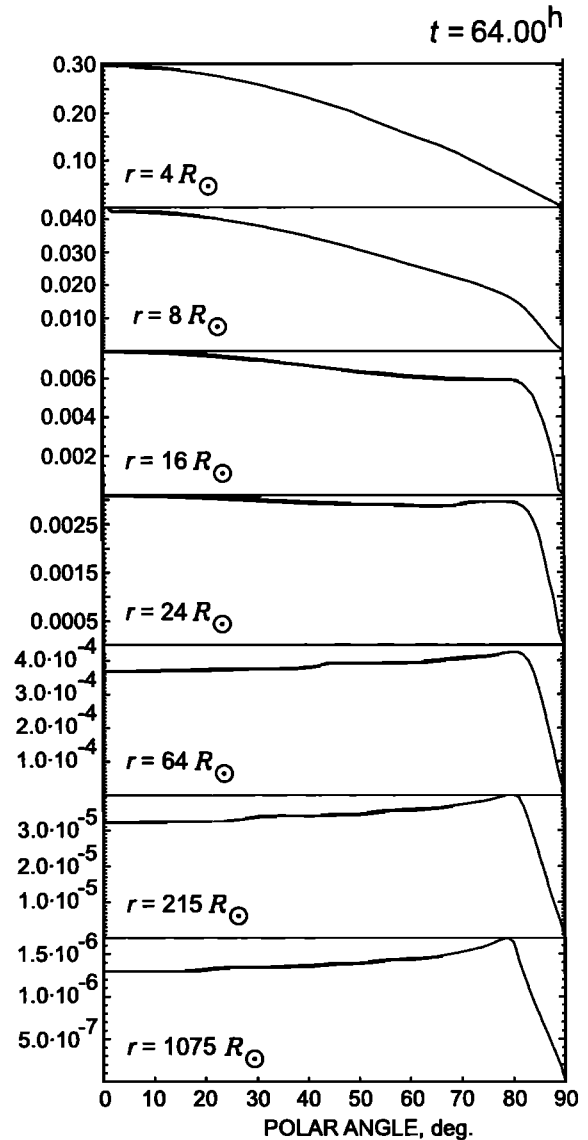


**Figure 11.** Latitudinal variations of the radial component of the magnetic field at radial distances from  $4 R_\odot$  to 5 AU (in gauss).



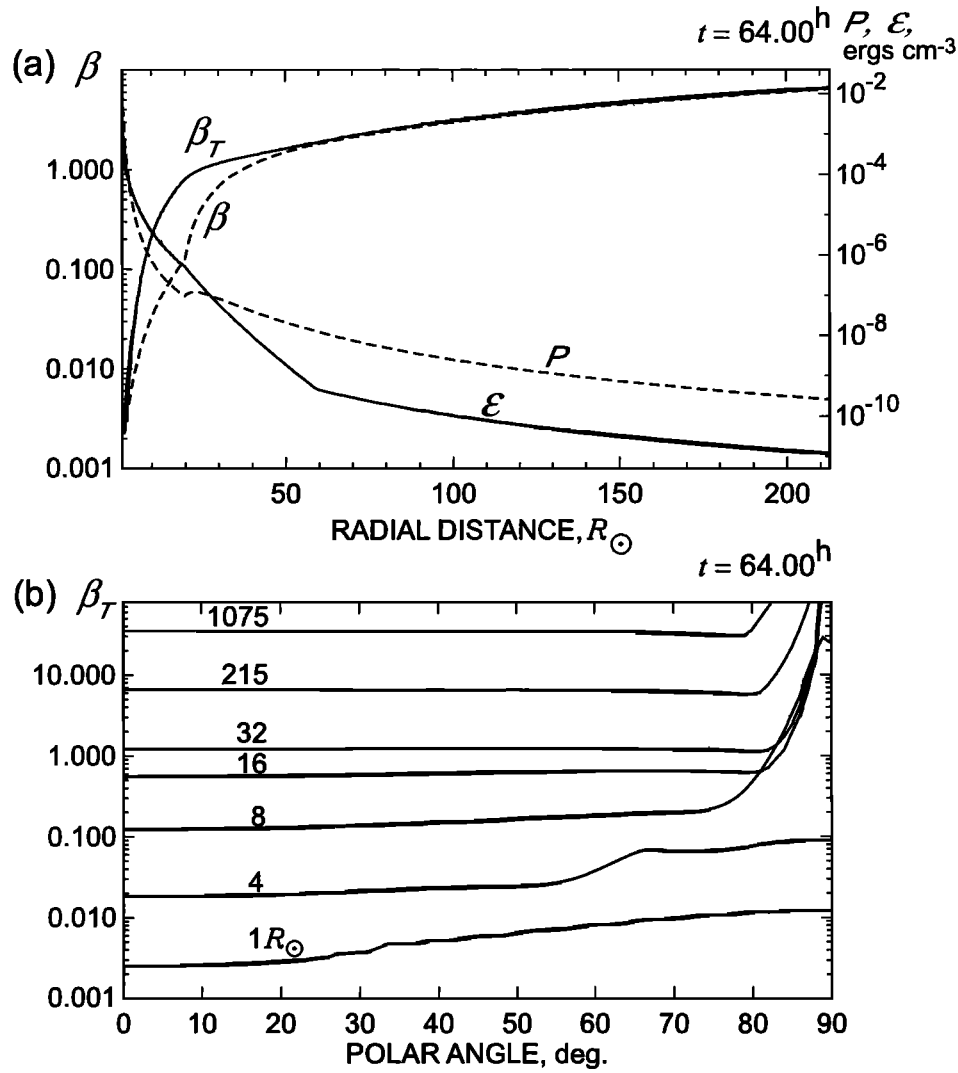


**Figure 12.** (a) Radial variations of thermal pressure  $P$ , Alfvén wave energy density  $\epsilon$ , plasma beta  $\beta$ , and a modified parameter  $\beta_T$  based on the sum of thermal pressure and wave energy density at  $\theta = 0^\circ$ . (b) The latitudinal variations of  $\beta_T$  at radial distances from  $1 R_\odot$  to 5 AU.

The dipole field strength ( $B_d$ ) (18 G at the pole) and the driven velocity amplitude of Alfvén waves ( $\delta V_M$ ) ( $35 \text{ km s}^{-1}$ ) at  $1 R_\odot$  were chosen to obtain a good fit to Ulysses observations of  $n$ ,  $T$ ,  $V$ , and  $B_r$  (similar results would be obtained for  $V$  if  $B_d$  were increased (decreased) and  $\delta V_M$  were decreased (increased), but the fit for  $B_r$ , especially, would not be as good). The results of our simulation demonstrate the formation of a bimodal structure consisting of fast and slow wind. The computed parameters are generally consistent with both solar wind and coronal parameters. We also note that while the solar wind acceleration is quite high in the near-Sun region ( $u_r \sim 400 \text{ km s}^{-1}$  at  $10 R_\odot$  and  $\sim 600 \text{ km s}^{-1}$  at  $20 R_\odot$ ), it is not as high as that reported by *Grall et al.* [1996] or as that suggested by the one-dimensional models of *McKenzie et al.* [1995] and *Esser et al.* [1997].

To compare our model with empirical data on solar wind speed and with another wave-driven solar wind

model, we show in Figure 14 the flow velocity along  $\theta = 0^\circ$  together with data from *Grall et al.* [1996, Figure 3]. Figure 14 reproduces measurements of the apparent flow velocity and the flow speed from the wave-driven one-dimensional model of *Esser et al.* [1986]. It is clear that for  $r > 20 R_\odot$  our model produces velocities  $\sim 100 \text{ km s}^{-1}$  higher than those from the model of *Esser et al.* (because of a higher wave energy influx at the coronal base) and matches closely the one-dimensional model at  $r \lesssim 10 R_\odot$  and the mean Ulysses velocity indicated with an arrow at  $100 R_\odot$ .

Our simulation study gives an insight into meridional dynamics of the expanding corona. We showed that two processes determine the meridional distribution of solar wind plasma and magnetic field parameters. The first one is dominant in the region where the meridional magnetic force dominates the thermal and wave energy gradients (in present model,  $\beta_T < 1$  if  $r < 24 R_\odot$ ). The Lorentz force produces equatorward plasma flows which

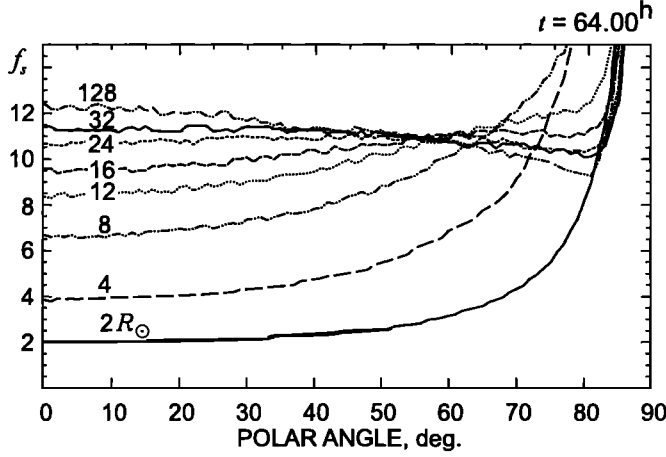


**Figure 13.** Latitudinal variations of the areal expansion factor between  $1 R_{\odot}$  and the radial distances up to 5 AU.

redistribute magnetic flux in latitude and creates a band of enhanced plasma densities near the equator. In combination with the outward streaming of coronal plasma this process leads to a relaxation of plasma and magnetic field gradients over most of the meridional flow, excepting only a relatively narrow band near the equator where those gradients are concentrated.

The relaxation ends where  $\beta_T \sim 1$  ( $r \sim 24 R_{\odot}$ ). The magnetic field strength, however, falls off with distance much faster than the thermal and wave energy gradients do, so that at  $r > 24 R_{\odot}$ , where  $\beta_T > 1$ , a second process begins; namely, the relaxation of the near-equatorial plasma concentration. This relaxation produces small poleward plasma motions which again redistribute magnetic flux and plasma in latitude and produce a slight poleward gradient in the radial velocity and an equatorward gradient in  $B_r$ . Our results on the meridional dynamics generally confirm those ob-

tained earlier from an analytical model by *Suess et al.* [1977], *Suess and Smith* [1996], and *Suess et al.* [1996]. The secondary relaxation process is, however, much less prominent in the present model than in the computations by *Suess et al.* and hence leads to a less noticeable secondary redistribution of magnetic flux in latitude.

Although this two-dimensional model agrees well with Ulysses observations of the latitudinal and radial distribution of magnetic field, plasma density, temperature, and speed, the model needs to be generalized to three dimensions so that warping of the HCS and departures from north-south symmetry [see, e.g., *Osherovich et al.*, 1999] can be included. A three-dimensional model is also essential for modeling the active Sun. Inclusion of Alfvén waves in a three-dimensional model would generalize the work of *Usmanov* [1993b, c]. Although we anticipate that a three-dimensional model would further improve the agreement with satellite observations, it may well be necessary to refine the treatment of coronal and solar wind heating. At present, we make no attempt to resolve the transition region where the temperature rises from  $\sim 10^4$  to  $\sim 10^6$  K [cf. *Hammer*, 1982], nor do we include a coronal heating mechanism. Such improvements will be deferred to future work.

## Appendix A: Solving One-Dimensional Equations for the Initial State

At the critical point  $r = r_c$ , we have from (23)

$$u_c^2 - c_{sc}^2 - u_{Ac}^2 = 0, \quad (\text{A1})$$

$$\frac{2(c_{sc}^2 + u_{Ac}^2)}{r_c} - \frac{GM_{\odot}}{r_c^2} - \left[ \left( \frac{3}{2} + \frac{V_{Ac}}{u_c} \right) (\gamma - 1) - \frac{\gamma}{2} \right] \frac{\mathcal{E}_c}{\rho_c L} = 0, \quad (\text{A2})$$

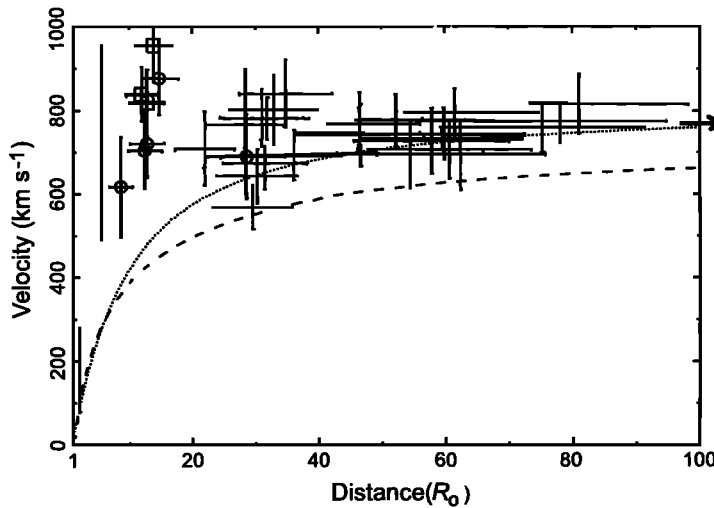


**Figure 14.** Radial velocity along  $\theta = 0^\circ$  (dotted line) from our model together with data from *Grall et al.* [1996, Figure 3], showing measurements of the apparent flow velocity. Also plotted is the flow velocity from the model of *Esser et al.* [1986] (dashed line).

where  $u_c$ ,  $\rho_c$ ,  $\mathcal{E}_c$ ,  $V_{Ac}$ ,  $c_{sc}$ , and  $u_{Ac}$  are the values of  $u_0$ ,  $\rho_0$ ,  $\mathcal{E}_0$ ,  $V_{Ar}^0$ ,  $c_{s0}$ , and  $u_{A0}$  at  $r = r_c$ . We assume that near the critical point,  $u_0 = u_c + a\Delta r$ , where  $a$  is the sought-for value of the velocity derivative and  $\Delta r = r - r_c \ll r_c$  is the distance from the critical point. In the vicinity of the critical point we have

$$\rho_0 = \rho_c \left[ 1 - 2\Delta r \left( \frac{1}{r_c} + \frac{a}{2u_c} \right) \right],$$

$$V_{Ar}^0 = V_{Ac} \left[ 1 - \Delta r \left( \frac{1}{r_c} - \frac{a}{2u_c} \right) \right],$$

$$\mathcal{E}_0 = \mathcal{E}_c \left\{ 1 - \Delta r \left[ \frac{1}{L} + \frac{3u_c + V_{Ac}}{u_c + V_{Ac}} \left( \frac{1}{r_c} + \frac{a}{2u_c} \right) \right] \right\},$$

$$c_{s0}^2 = c_{sc}^2 - \Delta r(\gamma - 1) \left[ au_c + \frac{GM_\odot}{r_c^2} - \left( \frac{3}{2} + \frac{V_{Ac}}{u_c} \right) \frac{\mathcal{E}_c}{\rho_c L} - 2u_{Ac}^2 \left( \frac{1}{r_c} + \frac{a}{2u_c} \right) \right],$$

$$u_{A0}^2 = u_{Ac}^2 - \Delta r \left[ \frac{u_{Ac}^2}{L} + J_1 \left( \frac{1}{r_c} + \frac{a}{2u_c} \right) \right],$$

$$J_1 = u_{Ac}^2 \frac{3u_c^2 - 4u_c V_{Ac} - V_{Ac}^2}{(u_c + V_{Ac})(3u_c + V_{Ac})}.$$

Then from (23) we obtain the following quadratic equation for  $a$ :

$$fa^2 + ga + h = 0, \quad (\text{A3})$$

where

$$\begin{aligned} f &= 2 - \frac{J_2}{u_c}, \quad g = -\frac{2J_2}{r_c} - \frac{J_4}{u_c}, \\ h &= -\frac{J_3}{L} - \frac{2}{r_c} \left( J_4 + \frac{GM_\odot}{r_c^2} - \frac{u_c^2}{r_c} \right), \\ J_2 &= (\gamma - 1) \left( \frac{u_{Ac}^2}{u_c} - u_c \right) - \frac{J_1}{2u_c}, \\ J_3 &= \left[ (\gamma - 1) \left( \frac{3}{2} + \frac{V_{Ac}}{u_c} \right) - \frac{\gamma}{2} \right] \frac{\mathcal{E}_c}{\rho_c L}, \\ J_4 &= (\gamma - 1) \left( \frac{2u_{Ac}^2}{r_c} - \frac{GM_\odot}{r_c^2} \right) - \frac{J_1}{r_c} + J_3 \\ &\quad + \frac{1}{L} \left( \frac{\gamma \mathcal{E}_c}{\rho_c} - 2u_{Ac}^2 \right). \end{aligned}$$

The algorithm to construct a solution proceeds by prescribing an initial value for the inflow boundary velocity  $u_0^S$ . We then compute  $r_c$  and  $u_c$  from (A1) and (A2) and find  $du_0/dr$  at  $r = r_c$  from (A3). We choose the positive root ( $a > 0$ ) at  $r = r_c$  (corresponding to a subsonic solution near the Sun and a supersonic solution at large distances). Starting from the critical point  $r_c$  and using  $u_c$  and  $a$ , we integrate in the sunward direction computing  $u_0(r)$  until we reach  $r = r_S$ . We vary the initial guess for  $u_0^S$  iteratively and repeat the calculations until we reach agreement between the initial guess and the value computed from the backward integration. At that point, we perform the integration in the supersonic flow region starting again from the critical point values.

## Appendix B: Numerical Techniques

We restrict our attention to solutions that are symmetric in  $\theta$  about the equator. In region I the computational domain covers  $1 \leq r \leq 20 R_\odot$  and  $-1^\circ \leq \theta \leq 91^\circ$ . The mesh points along  $r$  are distributed exponentially via  $r_i = r_1 \exp[(i-1)\Delta r']$ , where  $\Delta r' = 0.02$  and  $r_1 = 1 R_\odot$  ( $i = 1, \dots, 151$ ). The spacing of 93 mesh points along  $\theta$  is fixed to  $\Delta\theta = 1^\circ$ . The mesh points at  $\theta = -1^\circ$  and  $91^\circ$  are used to assign the symmetry boundary conditions [cf. *Steinolfson et al.*, 1982]. For the normalization (section 3.1) of dependent variables in (10)–(16), we use the functions  $\rho_0$ ,  $u_0$ ,  $P_0$ , and  $\mathcal{E}_0$  along the line  $\theta = 0^\circ$  and the function  $B_0 = B_d(r/r_S)^{-p}$ , where we choose  $p = 3$  because the initial magnetic field strength falls off with distance as  $r^{-3}$ .

To advance a solution of (10)–(16) in time from  $t$  to  $t + \Delta t$  ( $\Delta t$  is the time step) in region I and a solution of (17)–(22) from  $r$  to  $r + \Delta r$  ( $\Delta r$  is the step along radius) in region II, we use the numerical scheme of *MacCormack* [1971]. Additionally, an explicit artificial diffusion scheme [*Lapidus*, 1967] is used to maintain numerical stability in region I. In region II the numerical integration scheme is applied to the equations in conservation form and a transformation from the vector of conservation variables to the row variables is needed. The stability of the explicit *MacCormack* [1971] scheme in region I when taking into account artificial diffusion velocity is governed by the Courant-Friedrichs-Lewy (CFL) condition,  $\Delta t \leq \min(\Delta t_1, \Delta t_2)$ , where

$$\Delta t_1 \leq \min \left( \frac{\Delta r}{\max |\lambda_r^i|}, \frac{r \Delta \theta}{\max |\lambda_\theta^i|} \right),$$

$$\Delta t_2 \leq \min \left( \frac{0.5}{c_r \max |\partial u_r / \partial r|}, \frac{0.5}{c_\theta \max |\partial u_\theta / r \partial \theta|} \right),$$

and  $\lambda_r^i$  and  $\lambda_\theta^i$  ( $i = 1, \dots, 7$ ) are the characteristic velocities along the radial and meridional directions, respectively. The quantities  $\lambda_r^1 = u_r$ ,  $\lambda_r^{2,3} = u_r \pm V_{Ar}$ ,  $\lambda_\theta^1 = u_\theta$ ,  $\lambda_\theta^{2,3} = u_\theta \pm V_{A\theta}$ ,  $\lambda_r^{4,5,6,7}$  and  $\lambda_\theta^{4,5,6,7}$  are the algebraic roots of the fourth-order equations,

$$(u_r - \lambda_r)^4 - \left(c_s^2 + V_A^2 + \frac{3\mathcal{E}}{4\rho}\right)(u_r - \lambda_r)^2 + \frac{\mathcal{E}V_{Ar}}{2\rho}(u_r - \lambda_r) + V_{Ar}^2 \left(c_s^2 + \frac{\mathcal{E}}{4\rho}\right) = 0, \quad (\text{B1})$$

$$(u_\theta - \lambda_\theta)^4 - \left(c_s^2 + V_A^2 + \frac{3\mathcal{E}}{4\rho}\right)(u_\theta - \lambda_\theta)^2 + \frac{\mathcal{E}V_{A\theta}}{2\rho}(u_\theta - \lambda_\theta) + V_{A\theta}^2 \left(c_s^2 + \frac{\mathcal{E}}{4\rho}\right) = 0, \quad (\text{B2})$$

and  $c_s^2 = \gamma P/\rho$ . Note that if  $\mathcal{E} = 0$  then the usual magnetosonic velocities can be obtained from (B1) and (B2). The artificial diffusion velocity is governed by the non-dimensional constants  $c_r$  and  $c_\theta$ , which are measures of diffusion in the  $r$  and  $\theta$  directions, respectively [Lapidus, 1967]. In our simulation we choose  $c_r = 2$  and  $c_\theta = 4$ . The maximum allowable step size along the radial coordinate  $\Delta r$  in region II is also dictated by the CFL condition.

**Acknowledgments.** Ulysses plasma and magnetic field data were obtained from the NSSDC COHWeb. The authors would like to thank D. P. Stern for helpful comments. The research was made possible, in part, by grant RP1-191 from the U.S. Civilian Research and Development Foundation (CRDF).

Janet G. Luhmann thanks Steven T. Suess and another referee for their assistance in evaluating this paper.

## References

- Alazraki, G., and P. Couturier, Solar wind acceleration caused by the gradient of Alfvén wave pressure, *Astron. Astrophys.*, **13**, 380-389, 1971.
- Axford, W. I., and J. F. McKenzie, The origin of high speed solar wind streams, in *Solar Wind Seven: Proceedings of the 3rd COSPAR Colloquium held in Goslar, Germany, 16-20 September 1991*, edited by E. Marsch and R. Schwenn, pp. 1-5, Pergamon, Tarrytown, N. Y., 1992.
- Barnes, A., P. R. Gazis, and J. L. Phillips, Constraints on solar wind acceleration mechanisms from Ulysses plasma observations: The first polar pass, *Geophys. Res. Lett.*, **22**, 3309-3311, 1995.
- Belcher, J. W., Alfvénic wave pressures and the solar wind, *Astrophys. J.*, **168**, 509-524, 1971.
- Belcher, J. W., and L. Davis Jr., Large-amplitude Alfvén waves in the interplanetary medium, *J. Geophys. Res.*, **76**, 3534-3563, 1971.
- Belcher, J. W., L. Davis Jr., and E. J. Smith, Large-amplitude Alfvén waves in the interplanetary medium: Mariner 5, *J. Geophys. Res.*, **74**, 2302-2308, 1969.
- Bravo, S., and G. A. Stewart, Latitudinal variation of the heliospheric magnetic field during solar minimum, *Geophys. Res. Lett.*, **23**, 3271-3274, 1996.
- Coleman, P. J., Jr., Turbulence, viscosity and dissipation in the solar-wind plasma, *Astrophys. J.*, **153**, 371-388, 1968.
- Cuperman, S., L. Ofman, and M. Dryer, Thermally conductive magnetohydrodynamic flows in helmet-streamer coronal structures, *Astrophys. J.*, **350**, 846-855, 1990.
- Dorelli, J. C., and J. D. Scudder, Electron heat flow carried by Kappa distributions in the solar corona, *Geophys. Res. Lett.*, **26**, 3537-3540, 1999.
- Durney, B. R., and G. W. Pneuman, Solar-interplanetary modeling: 3-D solar wind solutions in prescribed non-radial magnetic field geometries, *Sol. Phys.*, **40**, 461-485, 1975.
- Endler, F., *Interaction between the solar wind and coronal magnetic fields*, Ph.D. thesis, Max-Planck-Institut für Physik und Astrophysik, Munich, Germany, 1971.
- Erdős, G., and A. Balogh, The symmetry of the heliospheric current sheet as observed by Ulysses during the fast latitude scan, *Geophys. Res. Lett.*, **25**, 245-248, 1998.
- Esser, R., E. Leer, S. R. Habbal, and G. L. Withbroe, A two-fluid solar wind model with Alfvén waves: Parameter study and application to observations, *J. Geophys. Res.*, **91**, 2950-2960, 1986.
- Esser, R., S. R. Habbal, W. A. Coles, and J. V. Hollweg, Hot protons in the inner corona and their effect on the flow properties of the solar wind, *J. Geophys. Res.*, **102**, 7063-7074, 1997.
- Feldman, W. C., B. L. Barraclough, J. L. Phillips, and Y.-M. Wang, Constraints on high-speed solar wind structure near its coronal base: A Ulysses perspective, *Astron. Astrophys.*, **316**, 355-367, 1996.
- Forsyth, R. J., A. Balogh, T. S. Horbury, G. Erdős, E. J. Smith, and M. E. Burton, The heliospheric magnetic field at solar minimum: Ulysses observations from pole to pole, *Astron. Astrophys.*, **316**, 287-295, 1996.
- Goldstein, B. E., and J. R. Jokipii, Effects of stream-associated fluctuations upon the radial variation of average solar wind parameters, *J. Geophys. Res.*, **82**, 1095-1105, 1977.
- Goldstein, M. L., D. A. Roberts, and W. H. Matthaeus, Magnetohydrodynamic turbulence in the solar wind, in *Annu. Rev. Astron. Astrophys.*, **33**, 283-325, 1995.
- Goldstein, M. L., D. A. Roberts, A. Deane, S. Ghosh, and H. K. Wong, Numerical simulation of Alfvénic turbulence in the solar wind, *J. Geophys. Res.*, **104**, 14,437-14,452, 1999.
- Gosling, J. T., S. J. Bame, W. C. Feldman, D. J. McComas, J. L. Phillips, B. Goldstein, M. Neugebauer, J. Burkepile, A. J. Hundhausen, and L. Acton, The band of solar wind variability at low heliographic latitudes near solar activity minimum: Plasma results from the Ulysses rapid latitude scan, *Geophys. Res. Lett.*, **22**, 3329-3332, 1995.
- Grall, R. R., W. A. Coles, M. T. Klingsmith, A. R. Breen, P. J. S. Williams, J. Markkanen, and R. Esser, Rapid acceleration of the polar solar wind, *Nature*, **379**, 429-432, 1996.
- Hammer, R., Energy balance of stellar coronae, I, Methods and examples, *Astrophys. J.*, **259**, 767-778, 1982.
- Hassler, D. M., G. J. Rottman, E. C. Shoub, and T. E. Holzer, Line broadening of Mg x  $\lambda\lambda 609$  and 625 coronal emission lines observed above the solar limb, *Astrophys. J.*, **348**, L77-L80, 1990.
- Heinemann, M., and S. Olbert, Non-WKB Alfvén waves in the solar wind, *J. Geophys. Res.*, **85**, 1311-1327, 1980.
- Hoeksema, J. T., *The Solar Magnetic Field 1985 through 1990: An Atlas of Photospheric Magnetic Field Observations and Computed Coronal Magnetic Fields from the John M. Wilcox Solar Observatory at Stanford 1985-1990*, Vol. 2, Rep. CSSA-ASTRO-91-01, Stanford Univ., Stanford, Calif., 1991.
- Hoeksema, J. T., and P. H. Scherrer, *An Atlas of Photospheric Magnetic Field Observations and Computed Heliospheric Magnetic Fields from the John M. Wilcox Solar Observatory at Stanford 1976-1984*, Rep. CSSA-ASTRO-85-11, Stanford Univ., Stanford, Calif., 1985.
- Hollweg, J. V., Alfvén waves in a two-fluid model of the solar wind, *Astrophys. J.*, **181**, 547-566, 1973.
- Hollweg, J. V., Some physical processes in the solar wind, *Rev. Geophys.*, **16**, 689-720, 1978.

- Hollweg, J. V., Status of solar wind modeling from the transition region outwards, in *Solar Wind Seven: Proceedings of the 3rd COSPAR Colloquium held in Goslar, Germany, 16-20 September 1991*, edited by E. Marsch and R. Schwenn, pp. 53-60, Pergamon, Tarrytown, N. Y., 1992.
- Holzer, T. E., T. Flå, and E. Leer, Alfvén waves in stellar winds, *Astrophys. J.*, **275**, 808-835, 1983.
- Hu, Y. Q., and S. T. Wu, A Full-Implicit-Continuous-Eulerian (FICE) scheme for multidimensional transient magnetohydrodynamic (MHD) flows, *J. Comput. Phys.*, **55**, 33-64, 1984.
- Hundhausen, A. J., *Coronal Expansion and Solar Wind*, 329 pp., Springer-Verlag, New York, 1972.
- Jacques, S. A., Momentum and energy transport by waves in the solar atmosphere and solar wind, *Astrophys. J.*, **215**, 942-951, 1977.
- Jacques, S. A., Solar wind models with Alfvén waves, *Astrophys. J.*, **226**, 632-649, 1978.
- Kopp, R. A., and T. E. Holzer, Dynamics of coronal hole regions, I, Steady polytropic flows with multiple critical points, *Sol. Phys.*, **49**, 43-56, 1976.
- Koutchmy, S., Study of the June 30, 1973 trans-polar coronal hole, *Sol. Phys.*, **51**, 399-407, 1977.
- Lapidus, A., A detached shock calculation by second-order finite differences, *J. Comput. Phys.*, **2**, 154-177, 1967.
- Lau, Y.-T., and E. Siregar, Nonlinear Alfvén wave propagation in the solar wind, *Astrophys. J.*, **465**, 451-461, 1996.
- Levine, R. H., M. D. Altschuler, and J. W. Harvey, Solar sources of the interplanetary magnetic field and solar wind, *J. Geophys. Res.*, **82**, 1061-1065, 1977.
- Linker, J. A., and Z. Mikić, Disruption of a helmet streamer by photospheric shear, *Astrophys. J.*, **438**, L45-L48, 1995.
- Linker, J. A., G. Van Hoven, and D. D. Schnack, A three-dimensional simulation of a coronal streamer, *Geophys. Res. Lett.*, **17**, 2281-2284, 1990.
- Linker, J. A., Z. Mikić, D. A. Biesecker, R. J. Forsyth, S. Gibson, A. J. Lazarus, A. Lecinski, P. Riley, A. Szabo, and B. J. Thompson, Magnetohydrodynamic modeling of the solar corona during Whole Sun Month, *J. Geophys. Res.*, **104**, 9809-9830, 1999.
- MacCormack, R. W., Numerical solution of the interaction of a shock wave with a laminar boundary layer, in *Proceedings of the Second International Conference on Numerical Methods in Fluid Dynamics, Lect. Notes Phys.*, vol. 8, edited by M. Holt, pp. 151-163, Springer-Verlag, New York, 1971.
- Matthaeus, W. H., and M. L. Goldstein, Stationarity of magnetohydrodynamic fluctuations in the solar wind, *J. Geophys. Res.*, **87**, 10,347-10,354, 1982.
- McKenzie, J. F., M. Banaszkiewicz, and W. I. Axford, Acceleration of the high speed solar wind, *Astron. Astrophys.*, **303**, L45-L48, 1995.
- McKenzie, J. F., W. I. Axford, and M. Banaszkiewicz, The fast solar wind, *Geophys. Res. Lett.*, **24**, 2877-2880, 1997.
- Mikić, Z., and J. A. Linker, The large-scale structure of the solar corona and inner heliosphere, in *Solar Wind 8: Proceedings of the Eighth International Solar Wind Conference*, edited by D. Winterhalter et al., *AIP Conf. Proc.*, **382**, 104-107, AIP Press, Woodbury, N. Y., 1996.
- Mikić, Z., J. A. Linker, D. D. Schnack, R. Lionello, and A. Tarditi, Magnetohydrodynamic modeling of the global solar corona, *Phys. Plasmas*, **6**, 2217-2224, 1999.
- Munro, R. H., and B. V. Jackson, Physical properties of a polar coronal hole from 2 to 5  $R_{\odot}$ , *Astrophys. J.*, **213**, 874-886, 1977.
- Nakagawa, Y., and R. S. Steinolfson, Dynamical response of the solar corona, I, Basic formulations, *Astrophys. J.*, **207**, 296-299, 1976.
- Ofman, L., and J. M. Davila, Alfvén wave heating of coronal holes and the relation to the high-speed solar wind, *J. Geophys. Res.*, **100**, 23,413-23,425, 1995.
- Ofman, L., and J. M. Davila, Solar wind acceleration by solitary waves in coronal holes, *Astrophys. J.*, **476**, 357-365, 1997.
- Ofman, L., and J. M. Davila, Solar wind acceleration by large-amplitude nonlinear waves: Parametric study, *J. Geophys. Res.*, **103**, 23,677-23,690, 1998.
- Ofman, L., V. M. Nakariakov, and C. E. DeForest, Slow magnetosonic waves in coronal plumes, *Astrophys. J.*, **514**, 441-447, 1999.
- Ong, K. K., Z. E. Musielak, R. Rosner, S. T. Suess, and M. E. Sulkanen, Self-consistent and time-dependent solar wind models, *Astrophys. J.*, **474**, L143-L145, 1997.
- Osherovich, V. A., J. Fainberg, R. R. Fisher, S. E. Gibson, M. L. Goldstein, M. Guhathakurta, and E. Siregar, The north-south coronal asymmetry with inferred magnetic quadrupole, in *Solar Wind Nine*, edited by S. R. Habbal, R. Esser, J. V. Hollweg, and P. A. Isenberg, pp. 721-724, AIP Press, Woodbury, N. Y., 1999.
- Parker, E. N., *Interplanetary Dynamical Processes*, Wiley-Interscience, New York, 1963.
- Parker, E. N., Solar and stellar coronae, *Adv. Space Res.*, **10**, (9), 17-29, 1990.
- Parker, E. N., Heating solar coronal holes, *Astrophys. J.*, **372**, 719-727, 1991.
- Phillips, J. L., et al., Ulysses solar wind plasma observations from pole to pole, *Geophys. Res. Lett.*, **22**, 3301-3304, 1995.
- Pizzo, V., A three-dimensional model of corotating streams in the solar wind, 3, Magnetohydrodynamic streams, *J. Geophys. Res.*, **87**, 4374-4394, 1982.
- Pizzo, V. J., and J. T. Gosling, 3-D simulation of high-latitude interaction regions: Comparison with Ulysses results, *Geophys. Res. Lett.*, **21**, 2063-2066, 1994.
- Pneuman, G. W., and R. A. Kopp, Gas-magnetic field interactions in the solar corona, *Sol. Phys.*, **18**, 258-270, 1971.
- Pneuman, G. W., S. F. Hansen, and R. T. Hansen, On the reality of potential magnetic fields in the solar corona, *Sol. Phys.*, **59**, 313-330, 1978.
- Roberts, D. A., Interplanetary observational constraints on Alfvén wave acceleration of the solar wind, *J. Geophys. Res.*, **94**, 6899-6905, 1989.
- Roberts, D. A., and M. L. Goldstein, Evidence for a high-latitude origin of lower latitude high-speed wind, *Geophys. Res. Lett.*, **25**, 595-598, 1998.
- Roberts, D. A., M. L. Goldstein, and L. W. Klein, The amplitudes of interplanetary fluctuations: Stream structure, heliocentric distance, and frequency dependence, *J. Geophys. Res.*, **95**, 4203-4216, 1990.
- Robertson, B. J., Self-consistent magnetohydrodynamic coronal hole flows, *Sol. Phys.*, **83**, 63-82, 1983.
- Ruderman, M., M. L. Goldstein, D. A. Roberts, and A. Deane, Alfvén wave phase mixing driven by velocity shear in three-dimensional open magnetic configurations, *J. Geophys. Res.*, **104**, 17,057-17,068, 1999.
- Schatten, K. H., J. M. Wilcox, and N. F. Ness, A model of interplanetary and coronal magnetic fields, *Sol. Phys.*, **6**, 442-455, 1969.
- Scime, E. E., S. J. Bame, W. C. Feldman, S. P. Gary, J. L. Phillips, and A. Balogh, Regulation of the solar wind electron heat flux from 1 to 5 AU: Ulysses observations, *J. Geophys. Res.*, **99**, 23,401-23,410, 1994.
- Sittler, E. C., and M. Guhathakurta, Semi-empirical two-dimensional magnetohydrodynamic model of the solar corona and interplanetary medium, *Astrophys. J.*, **523**, 812-826, 1999.

- Smith, E. J., and A. Balogh, Ulysses observations of the radial magnetic field, *Geophys. Res. Lett.*, **22**, 3317-3320, 1995.
- Smith, E. J., A. Balogh, M. E. Burton, G. Erdős, and R. J. Forsyth, Results of the Ulysses fast latitude scan: Magnetic field observations, *Geophys. Res. Lett.*, **22**, 3325-3328, 1995a.
- Smith, E. J., A. Balogh, M. Neugebauer, and D. McComas, Ulysses observations of Alfvén waves in the southern and northern solar hemispheres, *Geophys. Res. Lett.*, **22**, 3381-3384, 1995b.
- Smith, E. J., A. Balogh, R. P. Lepping, M. Neugebauer, J. L. Phillips, and B. T. Tsurutani, Ulysses observations of latitude gradients in the heliospheric magnetic field, *Adv. Space Res.*, **16** (9), 165-170, 1995c.
- Smith, E. J., A. Balogh, R. Forsyth, B. Tsurutani, and R. Lepping, Recent Ulysses observations of the heliospheric magnetic field, *Adv. Space Res.*, in press, 2000.
- Spitzer, L., Jr., *Physics of Fully Ionized Gases*, p. 144, Wiley-Interscience, New York, 1962.
- Steinolfson, R. S., S. T. Suess, and S. T. Wu, The steady global corona, *Astrophys. J.*, **255**, 730-742, 1982.
- Stewart, G. A., and S. Bravo, Self-consistent MHD modeling of the solar wind from polar coronal holes, in *Solar Wind 8: Proceedings of the Eighth International Solar Wind Conference*, edited by D. Winterhalter et al., *AIP Conf. Proc.*, **382**, 145-148, AIP Press, Woodbury, N. Y., 1996.
- Stewart, G. A., and S. Bravo, Latitudinal solar wind velocity variations from polar coronal holes: A self-consistent MHD model, *J. Geophys. Res.*, **102**, 11,263-11,272, 1997.
- Suess, S. T., and E. J. Smith, Latitudinal dependence of the radial IMF component: Coronal imprint, *Geophys. Res. Lett.*, **23**, 3267-3270, 1996.
- Suess, S. T., A. K. Richter, C. R. Winge, and S. F. Nerney, Solar polar coronal hole: A mathematical simulation, *Astrophys. J.*, **217**, 296-305, 1977.
- Suess, S. T., E. J. Smith, J. L. Phillips, B. E. Goldstein, and S. F. Nerney, Latitudinal dependence of the radial IMF component: Interplanetary imprint, *Astron. Astrophys.*, **316**, 304-312, 1996.
- Suess, S. T., A.-H. Wang, S. T. Wu, G. Poletto, and D. J. McComas, A two-fluid, MHD coronal model, *J. Geophys. Res.*, **104**, 4697-4708, 1999.
- Totten, T. L., J. W. Freeman, and S. Arya, An empirical determination of the polytropic index for the free-streaming solar wind using Helios 1 data, *J. Geophys. Res.*, **100**, 13-17, 1995.
- Tu, C.-Y., A solar wind model with the power spectrum of Alfvénic fluctuations, *Sol. Phys.*, **109**, 149-186, 1987.
- Tu, C.-Y., and E. Marsch, Two-fluid model for heating of the solar corona and acceleration of the solar wind by high-frequency Alfvén waves, *Sol. Phys.*, **171**, 363-391, 1997.
- Unti, T. W. J., and M. Neugebauer, Alfvén waves in the solar wind, *Phys. Fluids*, **11**, 563-568, 1968.
- Usmanov, A. V., Interplanetary magnetic field structure and solar wind parameters as inferred from solar magnetic field observations and by using a numerical 2-D MHD model, *Sol. Phys.*, **143**, 345-363, 1993a.
- Usmanov, A. V., A global numerical 3-D MHD model of the solar wind, *Sol. Phys.*, **146**, 377-396, 1993b.
- Usmanov, A. V., The global structure of the solar wind in June 1991, *Sol. Phys.*, **148**, 371-382, 1993c.
- Verma, M. K., D. A. Roberts, and M. L. Goldstein, Turbulent heating and temperature evolution in the solar wind plasma, *J. Geophys. Res.*, **100**, 19,839-19,850, 1995.
- Wang, A.-H., S. T. Wu, S. T. Suess, and G. Poletto, A two-dimensional MHD global coronal model: Steady-state streamers, *Sol. Phys.*, **147**, 55-71, 1993.
- Wang, A.-H., S. T. Wu, S. T. Suess, and G. Poletto, Global model of the corona with heat and momentum addition, *J. Geophys. Res.*, **103**, 1913-1922, 1998.
- Wang, S., Y. Q. Hu, and S. T. Wu, Full-Implicit Continuous Eulerian scheme in the spherical coordinates and its applications to solar phenomena, *Scientia Sinica Ser. A*, **25**, 1305-1318, 1982.
- Wang, Y.-M., Flux-tube divergence, coronal heating, and the solar wind, *Astrophys. J.*, **410**, L123-L126, 1993a.
- Wang, Y.-M., On the latitude and solar cycle dependence of the interplanetary magnetic field strength, *J. Geophys. Res.*, **98**, 3529-3537, 1993b.
- Wang, Y.-M., and N. R. Sheeley Jr., Solar wind speed and coronal flux-tube expansion, *Astrophys. J.*, **355**, 726-732, 1990.
- Wang, Y.-M., and N. R. Sheeley Jr., Solar implications of Ulysses interplanetary field measurements, *Astrophys. J.*, **447**, L143-L146, 1995.
- Washimi, H., Y. Yoshino, and T. Ogino, Two-dimensional structure of the solar wind near the sun, *Geophys. Res. Lett.*, **14**, 487-490, 1987.
- Whang, Y. C., and T. H. Chien, Expansion of the solar wind in high-speed streams, *Astrophys. J.*, **221**, 350-361, 1978.
- Withbroe, G. L., The temperature structure, mass, and energy flow in the corona and inner solar wind, *Astrophys. J.*, **325**, 442-467, 1988.
- Withbroe, G. L., The solar wind mass flux, *Astrophys. J.*, **337**, L49-L52, 1989.
- Wolfson, R., A coronal magnetic field model with volume and sheet currents, *Astrophys. J.*, **288**, 769-778, 1985.
- Zhao, X., and J. T. Hoeksema, Modeling of the out-of-ecliptic interplanetary magnetic field in the declining phase of sunspot cycle 22, *Space Sci. Rev.*, **72**, 189-192, 1995a.
- Zhao, X., and J. T. Hoeksema, Prediction of the interplanetary magnetic field strength, *J. Geophys. Res.*, **100**, 19-33, 1995b.
- Zhao, X., and J. T. Hoeksema, The temporal evolution of the radial component of the heliospheric magnetic field, in *Solar Wind 8: Proceedings of the Eighth International Solar Wind Conference*, edited by D. Winterhalter et al., *AIP Conf. Proc.*, **382**, 494-497, AIP Press, Woodbury, N. Y., 1996.

B. P. Besser and J. M. Fritzer, Space Research Institute, Austrian Academy of Sciences, Inffeldgasse 12, A-8010 Graz, Austria. (bruno.besser@oeaw.ac.at; johannes.fritzer@oeaw.ac.at)

M. L. Goldstein, Code 692, NASA Goddard Space Flight Center, Greenbelt, MD 20771. (melvyn.goldstein@gsfc.nasa.gov).

A. V. Usmanov, Institute of Physics, University of St. Petersburg, St. Petersburg 198904, Russia. (usmanov@snoopy.phys.spbu.ru).

(Received June 29, 1999; revised February 8, 2000; accepted February 8, 2000.)